INSTITUTO SUPERIOR TÉCNICO
Universidade Técnica de Lisboa

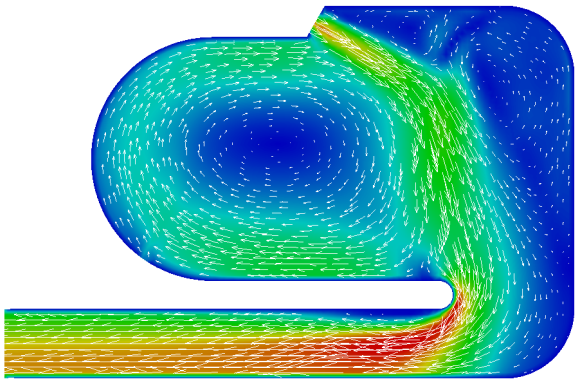

Characterization Of The Non-Reacting And Reacting Flow On A Low-NO_x GT Combustor With Enhanced Internal Mixing Mechanism

José Manuel das Neves Rodrigues

Dissertação para obtenção do Grau de Mestre em

Engenharia Aeroespacial

Júri

Presidente: Prof. Doutor Fernando José Parracho Lau (DEM)

Orientador: Prof. Doutor José Carlos Fernandes Pereira (DEM)

Vogal: Prof. Doutor Edgar Caetano Fernandes (DEM)

Dezembro 2011

ABSTRACT

The present work reports the numerical characterization of the non-reacting and reacting flow of a Low-NOx GT flameless combustor with intensive internal mixing mechanisms, for aircraft applications. From this analysis, the performance of the numerical model in reproducing the reacting flow and the mixing processes is highlighted. The unsteady flow was computed with two URANS turbulence models – the standard $k-\varepsilon$ and a RSTM model – and the PaSR combustion model, implemented in OpenFOAM®, with the skeletal Smooke chemical mechanism. The grid and the turbulence models effects on the numerical solution were also investigated and the results were compared with experimental data. In addition, the PaSR combustion model was tested and validated with a lifted turbulent diffusion flame test case, well documented in the literature. Three chemical mechanisms were used along the combustion model, namely the 2-step Westbrook and Dryer mechanism, the skeletal Smooke mechanism and the detailed GRI-2.11 mechanism. The results of the non-reacting flow showed good agreement with experimental data and exhibited little dependence from the grid or from the turbulence models used. The non-reacting flow features two recirculating regions, one of which being the large recirculating region holding chemical reactions and the other a parasite motion that had no relevant contribution for the aerodynamics of the combustor. The inlet jets force turbulence penetration into the reacting zone, improving the mixing mechanisms and, consequently combustion efficiency. The PaSR combustion model together with the turbulence models were insufficient to reproduce appropriately the reaction rates and species diffusion. Accordingly, the temperature field, either in the reacting flow inside the combustor or in the lift-off flame test were over-predicted Not withstanding, despite the poor correlation with the temperature measurements, the estimated reacting-flow inside the combustor yielded the fundamental working conditions appropriate for flameless combustion.

RESUMO

O presente trabalho apresenta a análise numérica do escoamento reactivo e não reactivo da câmara de combustão de uma turbina a gás com baixas emissões de NO_x e mecanismos de mistura intensivos. Desta análise, a capacidade do modelo numérico em reproduzir o escoamento reactivo e os mecanismos de mistura é avaliada. O escoamento transiente foi calculado com dos modelos de turbulência – o modelo $k - \varepsilon$ padrão e o modelo de transporte das tensões de Reynolds – e o modelo de combustão PaSR implementado no OpenFOAM® em conjunto com o mecanismo de reacções químicas simplificado de Smooke. Os efeitos da malha e dos modelos de turbulência na solução numérica são investigados e os resultados são comparados com medidas obtidas experimentalmente. O modelo de combustão PaSR foi testado e validado com uma chama de difusão descolada, descrita na literatura. Três esquemas de reações químicas foram usados para validar o modelo de combustão: o mecanismo de dois passos de Westbrook e Dryer, o mecanismo simplificado de Smooke e o mecanismo detalhado GRI-2.11. Verificou-se que os resultados do escoamento não reativo reproduziram os dados experimentais com precisão razoável, independentemente da malha ou dos modelos de turbulência usados. O escoamento não reactivo apresenta duas zonas de recirculação: uma região de recirculação que abrange grande parte do volume da câmara de combustão e alberga as reacções químicas e uma segunda zona de recirculação parasita que não é relevante para a performance aerodinâmica da câmara de combustão. Os jactos de entrada de ar forçam a penetração de turbulência na zona de reacção, melhorando os mecanismos de mistura e, consequentemente, melhorando a eficiência global da combustão. O modelo de combustão PaSR juntamente com os modelos de turbulência revelaram-se insuficientes no cálculo das taxas de reacção química e de difusão de espécies químicas. Consequentemente, o campo de temperaturas, tanto nos resultados do escoamento reactivo na câmara de combustão como na simulação da chama de teste, foram sobrestimados. Contudo, apesar da fraca concordância com os dados experimentais, a previsão do escoamento reactivo no interior da câmara de combustão evidenciou as características fundamentais necessárias para o regime de combustão sem chama visível.

KEYWORDS

Computational Fluid Dynamics

Flameless oxidation

FLOXCOM® combustor

Combustion models

Turbulence models

PALAVRAS-CHAVE

Dinâmica de Fluídos Computacional

Oxidação sem chama vísivel

Combustor FLOXCOM®

Modelos de combustão

Modelos de turbulência

ACKNOWLEDGEMENTS

I would like to express my sincere gratitude to my supervisors, Prof. José C. F. Pereira and Prof. Y. Levy for their continuous interest, support and guidance during this study.

To Prof. Y. Levy's team in the Turbo & Jet Propulsion Lab and to the LASEF team my genuine appreciation for welcoming me and, most of all, for their friendship.

I would like to thank Doctor Mário M. G. Costa and Doctor Mário J. F. R. V. Melo for generously providing valuable material for the realization of this work.

Finally, I dedicate this thesis to my friends and family with whom I have shared this important journey of my life.

TABLE OF CONTENTS

LIST OF FIGURES

LIST OF TABLES

NOMENCLATURE

Roman letters

$a_{\varepsilon,i}$	Radiative energy fraction emitted by a black body in the range of wavelengths in which the spectral absorption coefficient of the mixture is similar to the absorption coefficient of gas *i*
c	Unresolved molar concentration a reactor cell [kmol/m^3]
c_0	Molar concentration a reactor cell at the initial time-step [kmol/m^3]
c_1	Molar concentration a reactor cell at the final time-step [kmol/m^3]
c_p	Specific heat at constant pressure [J/kg.K]
$\vec{f}_{e,k}$	Body forces acting on each individual species *k* [N]
h_{LO}	Lift-off height [m]
h_s	Sensible specific enthalpy [J/kg]
k	Turbulent kinetic energy [m^2/s^2]
n	Normal distance to the wall in the RSTM model [m]
$\vec{n}$	Normal direction to the surface
p	Pressure [Pa]
q_R'''	Radiative heat source [W/m^3]
$\vec{q}$	Radiative heat flux [W/m^2]
r	Radial direction [m]
s	Mean path length [m]
$\vec{s}$	Vector ray
$\vec{s}'$	Vector of the incoming ray
t_0	Initial time-step [s]
t_1	Final time-step [s]
$\vec{u}$	Vector velocity [m/s]
u'	Velocity fluctuation in the axial direction [m/s]
v'	Velocity fluctuation in the radial direction [m/s]
w_j	Quadrature weight for direction *j*
x	Axial direction [m]
z	Axial direction [m]

$A_{f,j}$	Pre-exponential of the Arrhenius empirical law of reaction *j*
C_1, C_2, C_s, C_ε, $C_{1\varepsilon}$, $C_{2\varepsilon}$	RSTM turbulence model constants
C_μ, $C_{\varepsilon 1}$, $C_{\varepsilon 2}$, $C_{\varepsilon 3}$	Standard $k-\varepsilon$ turbulence model constants
C_{mix}	PaSR model constant
D	Inner diameter of the burner [m]
$D_{eff,k}^{M}$	Effective mass diffusion coefficient [m^2/s]
D_k^M	Mean molecular diffusion coefficient of species *k* [m^2/s]
D_R	Diameter of the recirculation zone [m]
E_j	Activation energy of reaction *j* [J/kmol]
$\vec{F}$	Flux of a generic conserved quantity
G	Incident irradiation [W/m^2]
I	Radiation intensity [$W/m^2.sr$]
I^n	Radiation intensity for direction n [$W/m^2.sr$]
I_b	Blackbody radiation intensity [$W/m^2.sr$]
I_{bw}	Blackbody radiation intensity at surface temperature [$W/m^2.sr$]
I_w	Radiation intensity leaving the surface [$W/m^2.sr$]
I_w^n	Blackbody radiation intensity for direction n [$W/m^2.sr$]
$\mathcal{J}$	Turbulent kinetic energy production terms due to buoyancy effects [$kg/m.s^3$]
$K_{f,j}$	Arrhenius reaction rates for the forward reaction
$K_{r,j}$	Arrhenius reaction rates for the reverse reaction
K_V	Recirculation rate
Le_k	Lewis number of species *k*
$\mathcal{M}_k$	Chemical symbol for species *k*
$\mathcal{P}$	Turbulent kinetic energy production tensor due to the mean velocity gradients [$kg/m.s^3$]
P_i	Partial pressure of gas *I* [Pa]
Pr_t	Turbulent Prandtl number
$\mathcal{Q}_j$	Rate of progress of reaction *j* [kmol/s]
$\vec{Q}_S$	Surface source/sink of a conserved quantity
Q_V	Volume source/sink of a conserved quantity

R	Universal gas constant [J/kmolK]
$Sc_{t,k}$	Turbulent Schmidt number of species *k*
T	Temperature [T]
T_0	Ambient temperature [K]
$\vec{V}_k$	Diffusion velocity vector of species *k* [m/s]
W_k	Molecular weight [kg/kmol]
Y_l^m	Spherical harmonics
Y_k	Mass fraction of species *k*

Greek letters

α	Thermal diffusivity coefficient [m^2/s]
$\hat{\alpha}$	RSTM turbulence model constant
α_{eff}	Effective thermal diffusion coefficient [m^2/s]
$\hat{\beta}$	RSTM turbulence model constant
β_j	Temperature exponent of the Arrhenius empirical law of reaction *j*
$\hat{\gamma}$	RSTM turbulence model constant
δ_{ij}	Kronecker symbol
ε	Turbulent kinetic energy dissipation rate [m^2/s^3]
ε_w	Surface emissivity
θ	Tangential direction [m]
κ	Reaction rate factor
κ^*	Reactive fraction of the reactor cell
κ_m	Medium absorption coefficient [m^{-1}]
λ	Thermal conductivity [W/m.K]
μ	Dynamic molecular viscosity [kg/m.s]
μ_{eff}	Effective dynamic viscosity [kg/m.s]
μ_t	Turbulent dynamic viscosity [kg/m.s]
ν'_{kj}	Molar stoichiometric coefficients of species *k* in reaction *j* for the forward reaction
ν''_{kj}	Molar stoichiometric coefficients of species *k* in reaction *j* for the reverse reaction
ρ	Density [kg/m^3]

ρ_w	Surface reflectivity
σ	Stefan-Boltzmann constant [W/m^3.K^4]
$\sigma_k, \sigma_\varepsilon$	Standard $k-\varepsilon$ turbulence model constants
τ_{op}	Optical distance
τ	Time-step [s]
$\bar{\bar{\tau}}$	Viscous shear stress tensor [Pa]
τ_c	Chemical timescale [s]
τ_{ij}	Reynolds-stress component
τ_{mix}	Turbulent mixing time [s]
$\dot{\omega}_k$	rate of production/consumption of species *k* [kg/m^3.s]
$\dot{\omega}_T$	heat release due to combustion [J/kg.s]
∇_τ	divergent operator written for the space coordinates nondimensionalized using the extinction coefficient
$\Delta h^o_{f,k}$	Mass enthalpy of formation at standard reference [J/kg]
Π_{ij}	Pressure-Strain correlation
Φ	Generic conserved quantity
Ω	Solid angle [sr]

Accents

$()''$	Favre decomposition fluctuation
$\widetilde{()}$	Favre-average or mass-average
$\overline{()}$	Reynolds average

ACRONYMS

CDC	Colorless Distributed Combustion
CFD	Computational Fluid Dynamics
CV	Control volume
DOM	Discrete Ordinates Method
EDC	Eddy Dissipation Concept
EDM	Eddy Dissipation Model
FLOX®	Flameless Oxidation
FLOXCOM®	Flameless Oxidation Combustor
GHG	Greenhouse Gases
GT	Gas Turbine
HITAC	High Temperature Air Combustion
IF	Industrial Furnace
IST	Instituto Superior Técnico
l.h.s	Left hand side
LDA	Laser Doppler Anemometry
LES	Large Eddy Simulation
MILD	Moderate and Intense Low Oxygen Dilution
MUSCL	Monotone Upstream-centered Schemes for Conservation Laws
ODE	Ordinary Differential Equations
OpenFOAM®	Open Field Operation And Manipulation
PaSR	Partially Stirred Reactor
PDE	Partial Differential Equation
PISO	Pressure Implicit Splitting of Operators
PSR	Perfectly stirred reactor
r.h.s	Right hand side
RANS	Reynolds Averaged Navier-Stokes
RSTM	Reynolds Stress Transport Model
UHC	Unburned Hydrocarbons
URANS	Unsteady Reynolds Averaged Navier-Stokes

CHAPTER 1

INTRODUCTION

1.1 Motivation

The massive release of greenhouse gases (GHG) to the atmosphere has been pointed out as the well-known reason for the climate change the Earth's ecosystem is facing today. The excessive emission of GHG and other toxic pollutants started when combustion of fossil fuels became the major source for power during the industrial revolution in the half end of the 19th century. In the last 160 years, GHG levels sky rose due to the wild consumption of fossil fuels for power production and transportation. Only by the last decade of the 20th century, scientists started alerting for this fact and for the severe consequences the high levels of GHG depleted to the atmosphere can inflict on climate and public health. According to the United Nations Framework Convention on Climate Change (UNFCCC, 2011), in 1990, about 76% of the total anthropogenic CO_2 was originated in the energy production, industrial manufacturing and transportation sectors. In 1993, in an international effort to mitigate this tendency, the Kyoto Protocol set targets for most industrialized countries to cut and maintain GHG emissions. As a result, in 2009, the UNFCCC reports a 5.1% reduction in CO_2 emissions for the same aforementioned sectors. Aircraft traffic contribution to the anthropogenic CO_2 emissions was around 2.4% in 2006, in the U.S. alone (U.S. Department of Transportation, 2010), but, with the increasing demand on air travel, this contribution keeps growing at a fast rate.

Carbon dioxide constitutes roughly 70% of the exhaust gases of a gas turbine (GT) used in aircraft propulsion and power generation, mainly. Even though it is considered a pollutant, CO_2 is a natural product of the complete oxidation of any carbon-based fuel and the only option to reduce emissions is to improve the thermodynamic cycle efficiency of every engine, burning less fuel. Better efficiency also means lower operating costs for the same performance so, therefore, it is of the highest interest to invest in new combustion technologies. Increasing pressure-ratio is a method generally used in gas turbines to improve cycle efficiency. However, this approach yields high flame temperatures due to the high inlet gas temperatures, promoting formation of nitrous oxides, NO_x – another hazardous pollutant threatening climate and human health. The same issue is present in industrial furnaces (IF) where inlet combustion air is preheated with the exhaust gases, by means of a heat exchanger, to improve thermal efficiency. Besides CO_2 and NO_x, carbon monoxide (CO), particulate matter (C), sulfur oxides (SO_x) and Unburned hydrocarbons (UHC) are among the most toxic elements also leaving the exhaust of a GT and IF. Over the last two decades, various researchers developed new methods for reduction and depletion of those gases and some methods are already certified and in use today. Still, although there are several proposed technologies for mitigation of NO_x during combustion, practical issues, high complexity, operating instabilities and excessive cost prevent such technologies to be accepted by engine manufacturers.

Globally, emissions from an aircraft GT account for roughly 3% of the total man-made NO_x and 2% are in the United States alone (Penner *et al.*, 2000). Even though this represents a modest amount, NO_x tends to accumulate near highly populated areas, such as a big city with a busy airport and airplanes hovering above it, waiting for their call for landing. Moreover, the highest NO_x emission rates are registered at takeoff phase, when the engine is at full-power. This accumulation of NO_x at ground level promotes formation of toxic ozone and smog, threatening public health and the well-being of the population.

NO_x (NO and NO_2) is produced in a combustor through four established mechanisms: the thermal NO, the prompt NO, the nitrous oxide mechanism and fuel NO (Lefebvre and Ballal, 2010). The latter two are of less importance for this study since they are little influenced by flame temperature or flame structure. The thermal NO mechanism is described by the oxidation of atmospheric nitrogen (N_2) in high-temperature regions of the flame and post-flame gases through the Zeldovich reaction scheme (Zeldovich *et al.,* 1947). This process is highly endothermic and evolves rapidly for temperatures above 1850 K. The prompt NO mechanism describes the formation of NO under fuel rich conditions, involving reactions

between hydrocarbons radicals (CH) and N_2. Prompt NO is usually found early in the flame region, near the burner, where the CH free radicals were just released from the main hydrocarbon chain.

1.2 State of the Art

Several researchers investigated new techniques to overcome the advert thermal NO_x formation when combustion air is pre-heated so to increase thermal efficiency. It was found that strong internal recirculation of hot combustion products proved to be an effective method to reduce flame temperature. The large concentration of combustion products increases the heat capacity of the gases in the reaction region of the combustor, reducing flame temperatures and maintaining a homogeneous temperature distribution. On the other hand, it also reduces the oxygen levels available in the reaction zone, and therefore, reaction rates decrease and combustion reactions will spread evenly over a large area. As a result, the species and temperature distribution in the reaction region are fairly uniform, yielding very smooth gradients. It is verified that the maximum temperature attained in these conditions is lower than 1850 K, avoiding large formation of thermal-NO. Furthermore, no luminosity or sound are emitted from the reaction zone and, for this reasons, this combustion regime is called flameless oxidation.

A high internal recirculation rate of exhaust combustion products is the basic principle of flameless oxidation. This statement is advocated by Wünning and Wünning in their work entitled *Flameless Oxidation to Reduce Thermal NO-Formation*, published in 1997, which sets the reference for this new and promising combustion technology. The authors found that recirculation rates much greater than the unity could hold stable combustion, only if the combustion chamber gases are brought to relatively high temperatures. Formerly, the maximum recirculation rate known to held stable combustion was only 0,5. Figure 1 shows a diagram first published in Wünning and Wünning (1997) identifying the stability limits for the different combustion modes as function of the recirculation rate and gas temperature inside the combustor. The recirculation rate, K_v, is defined in Wünning and Wünning (1997) as the ratio between the mass flow rate of recirculated exhaust gases and the sum of combustion air and fuel mass flux. In Figure 1, Zone A corresponds to a stable and attached flame. Combustion is held stable for any temperature of the gases inside the chamber but the recirculation rates are limited to 0.3 or 0.5 for higher temperatures. Crossing these limits to zone B, the flame becomes unstable, lifts-off and blows-off eventually. However, if the temperature of the recirculation gases is high enough (typically above 800 ºC, depending on

the fuel properties) and the recirculation rate as well ($K_v > 3$), the flameless oxidation mode is attained (zone C in the diagram). In a combustor operating inside domain C, the reaction rates are slowed down as enough burnt gases with high heat capacity dilute the combustion air to reduce the oxygen mass fraction of the reacting mixture. As a result, the reaction zone extends over a greater volume inside the combustor and the adiabatic temperature rise is far less than the rise found in a typical stable flame from zone A, with no recirculation. Accordingly, this combustion types require much longer residence times so that complete combustion can be assured. Further, Wünning and Wünning (1997) stated that stable flameless oxidation is possible for a low equivalent ratio mixture, far off the stoichiometric conditions. The mentioned properties are of utmost importance for flameless oxidation. On one hand, they make possible to control the temperature profile inside the combustor, even for highly preheated air, keeping temperatures below 1850 K and evenly distributed through out the reaction zone. This will favor the engine thermal efficiency without the advert effect of thermal NO formation. On the other hand, the use of lower equivalence ratios leads to better fuel efficiency. Another advantage lays on the fact that there are no moving parts necessary to this combustion technology since the recirculation mechanism is generated by the aerodynamics of the chamber alone. The flameless oxidation combustor, often referred as FLOX®, falls into the category of the ultra-low NO_x combustors, with NO_x emission levels sitting below the 10 ppm threshold.

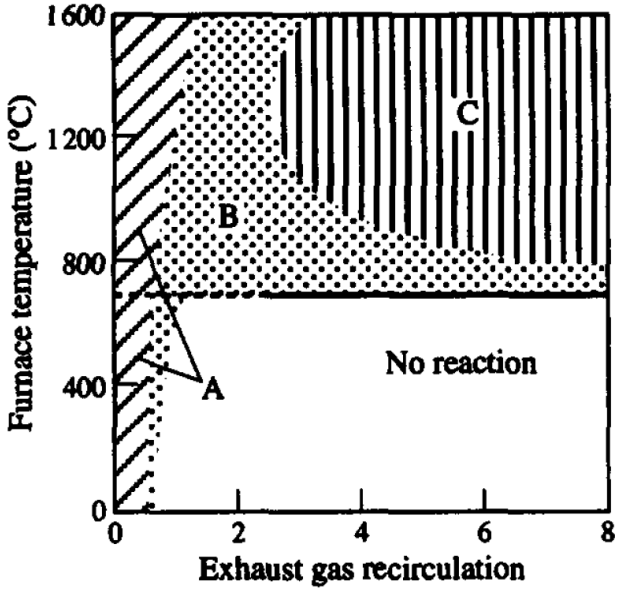

Figure 1 – Flame stability limits: A - stable flame, B - unstable flame, C - Flameless oxidation (Wünning & Wünning, 1997)

Since the publication of the work done by Wünning and Wünning (1997), several researchers studied this technology. Among them, there was the japanese Katsuki and Hasegawa (1998) who named this technology as HITAC (*high-temperature air combustion*), Joannon *et al.* (1999), who named it as MILD (*moderate and intense low oxygen dilution*) and, more recently, Arghode (2009) with his own designation being CDC (*colorless distributed combustion*).

Levy *et al.* (2004) proposed a novel combustor concept to achieve flameless combustion and with application to aircraft gas turbines – the FLOXCOM® adiabatic combustor. The geometry of the combustor was specially designed to improve the mixing capacity between the combustion air stream and the recirculating products and prepare a large, homogenous and vitiated mixture to hold the chemical reactions. Figure 2 illustrates the working principle of the FLOXCOM® combustor. Once the combustion products are well diluted in the new combustion air, fuel is injected and mixed with the reacting mixture at junction 3 in the scheme of Figure 2. An important requirement to attain flameless combustion is to avoid fuel injection before perfect dilution of air and burnt gases so that the oxygen content of the mixture is not too high the temperature is above the auto-ignition temperature of the fuel. Subsequently, provided that the vitiated mixture temperature exceeds the fuel auto-ignition temperature, the flammable mixture ignites spontaneously and continuous combustion is sustained.

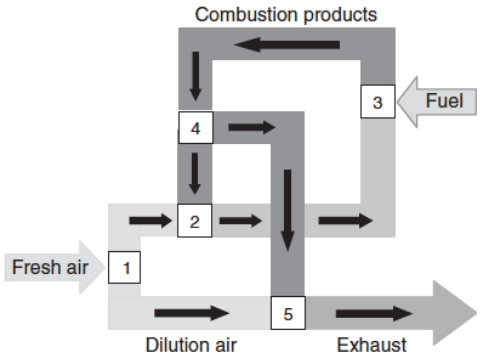

Figure 2 – Working principle of the combustor (Melo *et al.*, 2009)

In flameless regime, the temperature profile develops uniformly across the reaction zone, with the maximum temperature being typically lower than 1850 K and temperature gradients not higher than 200 K. Accordingly, no strong species gradients are detected, and the heat of combustion is evenly released through the reaction region. At junction 4, part the combustion products are recirculated back to the reaction region (junction 2) and the remaining leaves the

combustor through the exhaust (junction 5). To cool down the hot exhaust gases, part of the fresh air inlet stream is directed straight to the dilution channel. This is an important requirement for GT combustors since the hot exhaust gases can seriously wear out the first stage turbine blades.

Figure 3 illustrates the cross-section of a combustor based on the FLOXCOM® concept, with dimensions and a schematic representation of the flow.

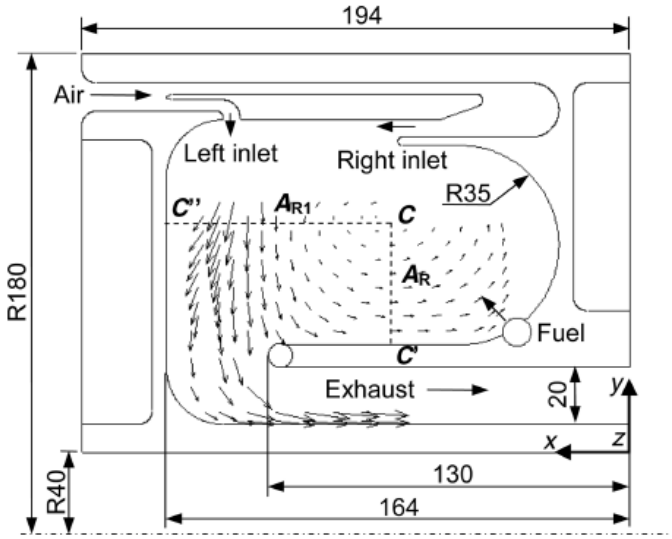

Figure 3 – Cross-section, flow schematics and key dimensions of a FLOXCOM® combustor (Melo *et al*,. 2009)

The small arrows in Figure 3 represent the recirculation zone, characterized as a large toroidial vortex movement of the flow, centered roughly at point C and occupying most of the combustor volume. This is typically where combustion occurs. As described in Levy, *et al* (2004), the air stream entering the combustor by both Left and Right inlet jets is split in two streams: the combustion air and the dilution air. This corresponds to junction 1 in the diagram of Figure 2. The combustion air stream is dragged into the recirculation zone, as shown by the flow schematics in Figure 3, and, subsequently, stirred with the hot burnt gases (junction 2). Fuel is added to the combustion air-burnt products mixture as it reaches the fuel inlet (junction 3), where fuel is being injected at a constant rate. Immediately, the mixture becomes inflammable and ignites if the flammable mixture temperature exceeds the auto-ignition temperature of the fuel. The resulting combustion products, heading back to the entrance of the combustor, are partially dragged to the dilution channel and the rest is recirculated back to the reaction zone (junction 4). Finally, the dilution air flowing towards the combustor outlet

dilutes the hot combustion products leaving the combustor, reducing their temperature and homogenizing the outlet temperature profile to prepare the gases to enter in the turbine. An important issue of the present design relates to the fact that the latter splitting mechanism, the mixing mechanisms and products recirculation are controlled exclusively by aerodynamic phenomena, which are still quite unknown. Melo *et al.* (2006 and 2009), studied these processes experimentally in six different combustor prototypes based on the FLOXCOM® concept with methane as fuel. The size of the inlet jets and their relative position inside the combustor were changed for each combustor prototype. Plus, Melo (2006) tested each combustor at different operating conditions, playing mainly with the combustion air mass flux and equivalence ratios. Melo (2006) concluded that recirculation rates depend on the inlet geometry, but are fairly insensible to the jets mass flux. Furthermore, he was able to sustain stable combustion for recirculation rates ranging from 0.4 to 1 and equivalence ratios as low as 0.2. Very low NO_x emissions were detected for all configurations, and, in most cases, concentrations below 10 ppm were attained, regardless the operating conditions. However, very high concentration of CO and HC at the outlet revealed that an insufficient residence time prevented complete combustion, resulting in low combustion efficiency for some configurations. Nonetheless, combustion efficiencies close to 1 (≈0.99) were also registered in one configuration. The study further reports an uniform temperature profile in the combustion zone, with gradients not higher than 200 K, very low oxygen concentration and temperatures not higher than 1850 K, endorsing the principles of flameless combustion.

The concept of flameless oxidation described before requires further developments in order to improve performance and reliability of that combustion mode. Computational Fluid Dynamics (CFD) currently offers great potential for application of their capabilities to study the flow mechanisms that most of the times are hidden from the experimentalist. Besides, it delivers a more comprehensive perspective over the flow, which helps understanding the overall mechanisms governing it. Furthermore, CFD is a convenient design tool, in the sense that it reduces prototyping costs and it is capable to simulate new design modifications with ease. On the other hand, the verification and validation of the CFD solution is mandatory since many modeling or numerical issues may induce large solution errors.

Several researchers have studied flameless combustion numerically, mostly on simple set-ups like industrial furnaces. However, there is still little research on this matter concerning GT applications, specially when complex and high intensity mixing mechanisms are involved. Typically, the *flamelets* combustion models, the eddy dissipation model (EDM) (Magnussen and Hjertager, 1976) and the eddy dissipation concept model (EDC) (Gran & Magnussen,

1996) are the preferred combustion models in most investigations. It was found that the EDC model combined with a detailed chemical mechanism offers the best matching results with experimental data and that the *flamelets* model is inappropriate to model the flameless combustion regime. In fact, the *flamelets* models are based on the assumption that the chemical timescale is much lower than the turbulent timescales (large Damköhler numbers), whereas the chemical and turbulent time scales in flameless combustion are of the same order of magnitude, corresponding to a Damköhler number close to unity. Furthermore, the *flamelets* model neglects the effect of the turbulent flow on the flame structure. Decoupling both phenomena in the mathematical formalism constitutes a very abusive assumption, provided that turbulence and combustion processes are strongly coupled. In the EDC model formulation, on the other hand, the chemistry and the turbulence phenomena are coupled to better reproduce the chemistry/turbulence interaction on the flame structure.

Most researchers agree that the standard k-ε turbulence model constitutes a compromise between its numerical simplicity and the Physical complexity of turbulent combustion. They found that the k-ε model is suitable to resolve the turbulence quantities for flameless combustion in an industrial furnace set-up and low recirculation rates. Moreover, some argue that the solution may be optimized if one modifies the $C_{1\varepsilon}$ model constant to 1.6, instead of the standard value 1.44 (Christo and Dally, 2005). Nevertheless, the standard k-ε turbulence model fails to reproduce the experimental data in the regions near the burner, where the flow gradients are higher (Rodi, 1984). This observation foretells a performance reduction of the standard k-ε model if strong and more efficient mixing mechanisms are introduced in the flow.

The present work focuses on the numerical analysis of the flow pattern inside a combustor based on the FLOXCOM® combustor concept, analyzed experimentally by Melo (2006). For that purpose, a CFD package named OpenFOAM® was used. OpenFOAM® stands for Open Field Operation And Manipulation (OpenCFD, 2011). This CFD toolbox is available license-free, although its capabilities are similar to a regular commercial CFD package. Besides, as the source code is open to the regular user, it can be easily expanded and customized with no extra cost. The code has a large and still growing user base, spanning from areas of engineering to science, in both academic and commercial organizations. The provided package offers a wide variety of solvers that handle the most complex fluid flows, including several turbulence models, chemical reactions and combustion models, radiation, electromagnetics and others. It is also includes solid dynamic solvers and even a solver for the

financial Black-Scholes equation to evaluate the price of commodities. Nevertheless, it can always be expanded to include user-created solvers. In fact, this software package is fully open, meaning that not only the source code is available, but also all its the structure and hierarchical design. Furthermore, the core of OpenFOAM® consists of a set of flexible C++ modules that can be put together in a very easy and efficient way, in order to build new solvers, physical models or utilities. OpenFOAM® handles 3D polyhedral grids exclusively and uses the finite volume method to discretize them. Axisymmetric, 2D and 1D grids are also emulated in OpenFOAM®, by setting a specific boundary condition to the computational domain faces normal to the direction of no interest. The strong feature of OpenFOAM® is parallelization. The code includes parallelization in a fundamental level, meaning that all solvers, models and utilities built with OpenFOAM® libraries have parallelization enabled. Also, it provides the utilities necessary to decompose and reconstruct the parallelized domain. Therefore, parallelization in OpenFOAM® is straightforward and very easy to use.

1.3 Objectives

In this work, we evaluate the numerical solution of the non-reacting and reacting flow characteristics of a combustor prototype based on the FLOXCOM® combustor concept, with enhanced internal mixing mechanism and designed to operate in flameless oxidation regime. The numerical results are compared with the experimental data measured and published in Melo (2006). The purpose for the non-reacting flow investigation of the flow is to study the complex flow mechanisms and mixing capabilities. Further, we validate the combustion model and chemistry/turbulence interaction model present in OpenFOAM® with a lift-off non-premixed flame studied by Mahmud, *et al.* (2007). Finally, the same combustion model is used to simulate the flameless oxidation regime in the same combustor prototype. The results are compared with data published in Melo (2006) and the performance of the numerical set-up in modeling the flameless combustion regime is discussed.

1.4 Structure of Thesis

The present dissertation work is organized in 4 chapters. The second chapter presents the flow equations that mathematically model the reacting and non-reacting flow. The conservation law equations and the Favre-averaged flow equations are listed and followed by the description of the turbulence models. Then, the turbulence/chemistry interaction model implemented in OpenFOAM® is introduced. This chapter ends with a brief description of two methods to compute the radiative heat fluxes. Chapter three reports the results obtained. The

first set of results refers to the isothermal investigation of the flow in the FLOXCOM® combustor. The grid effect and the turbulence effect on the solution are investigated as well. Following, the next section shows the validation results of the combustion model in OpenFOAM® with a lifted turbulent jet flame. Finally, the results of the reacting flow simulation of the FLOXCOM® combustor are presented and discussed. The last chapter comprises the closing conclusions and future work suggestions.

CHAPTER 2

NUMERICAL MODELING OF REACTING FLOW

The mathematical description of the reactive flow is presented in this section. We start by introducing the fundamental equations of fluid flow – mass, momentum and energy conservation – applied to reactive systems. Following, we describe the turbulent models used here to solve the turbulent fluctuations and close the averaged fluid flow equations. The standard k-ε model and the Reynolds Stress Turbulent Model (RSTM) were the turbulent models implemented for this investigation.

Further, combustion is treated with a turbulence/chemistry interaction model – the Chalmers PaSR model – and a chemistry solver to compute the Arrhenius reaction rate of each reaction of the chemical mechanism. Their mathematical description is presented.

To finish this section, the determination of the radiation source term of the energy conservation equation is presented. It was used the Method of the Discrete Ordinates and a particularization of the method of spherical harmonics, the P_1-approximation.

2.1 Conservation Laws of Fluid Flow

Fluid flows are completely characterized by the conservation of only three quantities: Mass, Momentum and Energy. Considering the Eulerian description of the fluid domain, the application of the conservation law to each of these quantities leads to the fundamental governing equations of fluid flow. Mass conservation law is expressed by the continuity equation, the Navier-Stokes equations result from the application of conservation law to momentum, whereas the energy equation accounts for conservation of total energy.

The differential form of the conservation law for a generic quantity Φ applied to an infinitesimal control volume is given by

$$\frac{\partial \Phi}{\partial t} + \vec{\nabla}.\vec{F} = Q_V + \vec{\nabla}.\vec{Q}_S \tag{2.1}$$

where $\vec{F}$ represents the flux of the quantity Φ entering and leaving the control volume (CV) and Q_V and $\vec{Q}_S$ are the volume and surface sources/sink of quantity Φ, respectively.

2.1.1 Continuity equation

The law of mass conservation is a formal translation of the empirical fact that in a fluid system, mass is never destroyed nor created. For this fact, mass can only be transported and, therefore, mass conservation is exclusively related to the kinematic state of the flow. Mass is transported exclusively by convection and no diffusive flux of mass exists. The mass conservation law equation in a differential form is given as follows:

$$\frac{\partial \rho}{\partial t} + \vec{\nabla}.(\rho\vec{u}) = 0 \tag{2.2}$$

This equation is better known as the *continuity equation*. The differential form is more convenient, from the numerical point of view, since the numerical domain is discretized in small elements, to an extent that infinitesimal theory can be applied.

2.1.2 Mass Conservation of Species

In reacting flows, even though the total mass of the reacting mixture is always conserved, each individual species in that mixture are consumed or produced at a certain rate, altering the mass balance for each one. Neglecting the diffusion caused by pressure gradients and the

Soret effect, molecular diffusion is approximated by Fick's law, $\vec{F}_{diff} = -\rho D_k^M \nabla Y_k$, where D_k^M is the mean molecular diffusion coefficient of species k in the mixture. Using this approximation, one can apply the scalar conservation law (equation (2.1)) to the mass fraction of any species k in the mixture, Y_k, giving the mass conservation equation for species k:

$$\frac{\partial \rho Y_k}{\partial t} + \nabla.(\rho \vec{u} Y_k) = \nabla.\left(\rho D_k^M \nabla Y_k\right) + \dot{\omega}_k \tag{2.3}$$

where $\dot{\omega}_k$ is a source/sink term representing the rate of production/consumption of species k, in kg/m^3.s.

2.1.3 Navier-Stokes equations

Momentum is another conserved quantity in fluid flows and is a vector quantity defined by the product of density by velocity, $\rho\vec{u}$. Therefore, the momentum conservation law can be obtained by using the general conservation law given in equation (2.1) and, after some algebraic manipulation, it yields:

$$\rho \frac{\partial \vec{u}}{\partial t} + \rho(\vec{u}.\nabla)\vec{u} = -\nabla p + \nabla.\bar{\bar{\tau}} + \rho \sum_{k=1}^{N} Y_k \vec{f}_{e,k} \tag{2.4}$$

In equation (2.4), the first term represents the transient variation of momentum in the infinitesimal CV. The convection term is expressed by the second term on the l.h.s, whereas the source terms are organized on the r.h.s. The last term represents the sum of the body forces acting on each individual species. The pressure term represents the effect of the flow pressure acting normally to the CV boundaries. The remaining term refers to the viscous forces. For a *Newtonian* fluid, the viscous shear stress tensor, $\bar{\bar{\tau}}$, is given as follows:

$$\tau_{ij} = \mu\left[\left(\frac{\partial u_j}{\partial x_i} + \frac{\partial u_i}{\partial x_j}\right) - \frac{2}{3}\frac{\partial u_k}{\partial x_k}\delta_{ij}\right] \tag{2.5}$$

Rewriting equation (2.4) with equation (2.5) leads to the *Navier-Stokes equations of motion*. Despite no explicit reaction terms are included on the *Navier-Stokes equations* in reacting flows, the momentum is strongly influenced by high temperature gradients, particularly in combustion, due to the very exothermic chemical reactions. In fact, with temperature gradients in the order of 1:8 or 1:10, density, dynamic viscosity, μ, and hence the Reynolds number also change significantly, with the flow behavior changing drastically.

2.1.4 Energy equation

The energy equation written in terms of the sensible specific enthalpy, h_s, is given by

$$\rho \frac{Dh_s}{Dt} = \dot{\omega}_T + \frac{Dp}{Dt} + \nabla.\left(\frac{\lambda}{c_p}\nabla h_s\right) - \nabla.\left[\sum_{k=1}^{N}\left(1 - \frac{1}{Le_k}\right)\frac{\lambda}{c_p}h_{s,k}\nabla Y_k\right] + \nabla.(\bar{\bar{\tau}}.\vec{u}) + q_R''' + \rho\sum_{k=1}^{N} Y_k\left(\vec{f}_{e,k}.\vec{V}_k\right) \tag{2.6}$$

where $\dot{\omega}_T = -\sum_{k=1}^{N}\Delta h_{f,k}^{o}\,\dot{\omega}_k$ is the heat release due to combustion, $\Delta h_{f,k}^{o}$ is the mass enthalpy of formation at standard reference conditions for species k and q_R''' is the radiative heat source term. The third and fourth terms on the r.h.s of equation (2.6) account for the heat vector flux due to conduction (Fourier's law) and mass diffusion, accordingly. Le_k is the Lewis number of species k and λ is the thermal conductibility. The last term of equation (2.6) refers to the contribution of the work done by volume forces $\vec{f}_{e,k}$ on each individual species, per unit volume. The sensible enthalpy, h_s, is evaluated as a *total derivative*, D/Dt, which is defined by the relation

$$\frac{D\Phi}{Dt} = \frac{\partial\Phi}{\partial t} + \vec{u}.\nabla\Phi \tag{2.7}$$

where Φ is an arbitrary conserved quantity.

For a reactive system where the work of the viscous and volume forces can be neglected, the flow Mach number is low enough to assume constant pressure and considering the molecular diffusivity equal to the thermal diffusivity (unit Lewis number) for every species, the enthalpy equation can be simplified to

$$\rho \frac{Dh_s}{Dt} = \dot{\omega}_T + \nabla.(\rho\alpha\nabla h_s) + q_R''' \tag{2.8}$$

where $\alpha = {}^{\lambda}/_{\rho c_p}$ is the thermal diffusivity coefficient.

2.2 Chemical Kinetics

The rate of consumption/production of species k, $\dot{\omega}_k$, is dictated by the chemical kinetics of the reaction system present in the reacting flow. A chemical system with N species reacting through M chemical reactions can be expressed as:

$$\sum_{k=1}^{n} \nu'_{kj} \mathcal{M}_k \Leftrightarrow \sum_{k=1}^{n} \nu''_{kj} \mathcal{M}_k \qquad \text{for } j = 1, M \tag{2.9}$$

where $\mathcal{M}_k$ is the chemical symbol for species k, ν'_{kj} and ν''_{kj} are the molar stoichiometric coefficients of species k in reaction j for the forward reaction and reverse reaction, accordingly. The consumption/production rate of species k, $\dot{\omega}_k$, is, therefore, defined by the sum of all the consumption/production rates of species k in each j reaction, that is:

$$\dot{\omega}_k = \sum_{j=1}^{M} \dot{\omega}_{kj} = W_k \sum_{j=1}^{M} \nu_{kj} \mathcal{Q}_j \tag{2.10}$$

where $\nu_{kj} = \nu''_{kj} - \nu'_{kj}$, W_k is the molecular weigth and $\mathcal{Q}_j = \frac{\dot{\omega}_{kj}}{W_k \nu_{kj}}$ is the rate of progress of reaction j defined by

$$\mathcal{Q}_j = K_{f,j} \prod_{k=1}^{N} [X_k]^{\nu'_{kj}} - K_{r,j} \prod_{k=1}^{N} [X_k]^{\nu''_{kj}} \tag{2.11}$$

where $K_{f,j}$ and $K_{r,j}$ are the Arrhenius reaction rates for the forward and reverse reaction. These reaction rates are modeled by the empirical Arrhenius law, which is given by

$$K_{f,j} = A_{f,j} T^{\beta_j} \exp\left(-\frac{E_j}{RT}\right) \tag{2.12}$$

The model constants – the pre-exponential, A, the temperature exponent, β, and the activation energy, E – are determined experimentally for each reaction j and must be provided in the chemistry mechanism. The fuel considered in this study was methane (CH_4) and three chemical mechanisms were employed to describe the oxidation of the methane-air flames: the simplified Westbrook and Dryer two-step mechanism (Westbrook and Dryer, 1981), with 2 equations and 5 species; the skeletal methane mechanism of Smooke (Smooke, 1991), with 33 equations and 17 species; and the detailed GRI-MECH 2.11 (Smith *et al.,* http://www.me.berkeley.edu/gri_mech/), with 277 elementary chemical reactions and 49

species. The GRI-MECH 2.11 mechanism includes nitrogen chemistry relevant to methane chemistry.

2.3 Turbulence Modeling

Turbulence is present in most practical applications involving fluid flow with sufficiently large Reynolds number, namely in GT and IF. The elementary flow structure of a turbulent flow is the eddy, which is a vortice-like structure generated by the viscous shear stress between flow layers. Eddies transport local flow properties, enhancing the mixing capacity of the flow in reacting flows. This characteristic is interesting for diffusion flames, increasing the contact area between fuel and oxidant, and, therefore, improving the combustion performance.

Turbulent motions require very high temporal and space resolutions to be reproduced with the equations of fluid motions presented in the last section, which, from the numerical point of view, is unfeasible for most applications of practical interest and require a significant amount of computational power. The Reynolds Averaged Navier-Stokes (RANS) is a simplified approach to the turbulence problem in which only the time-average of all properties is solved, whereas the turbulent shear stress are modeled with empirical relations, i. e., with the turbulence models. The Favre decomposition of flow quantities, based on a mass-average rather than a time-average, is preferable to use with compressible and reactive flow and is described below. In this investigation we used the $k-\varepsilon$ standard model and a Reynolds Stress Transport Model (RSTM) to model the turbulent fluctuations.

2.3.1 Averaged equations

The value of a flow quantity φ in a turbulent flow oscillates at every instant around a mean value. Numerically, it can be decomposed in two components: the mean value, $\tilde{\varphi}$, and a perturbation or fluctuation, φ'' such that

$$\varphi = \tilde{\varphi} + \varphi'' \tag{2.13}$$

where the mean value $\tilde{\varphi}$ is the mass-averaged of quantity φ and evaluated by

$$\tilde{\varphi} = \frac{1}{\bar{\rho}} \lim_{T\to\infty} \int_{t}^{t+T} \rho(x,\tau)\, \varphi(x,\tau) d\tau \tag{2.14}$$

where the over-bar represents the time-averaged of that quantity (Wilcox, 2006). This decomposition is called Favre decomposition and is preferably used for compressible flows, since the Reynolds time-average decomposition adds a density fluctuation term to the continuity equation, acting as a numerical source, which, therefore, violates mass conservation. Applying Favre decomposition to the flow quantities – $\vec{u}$, ρ, p, h_s and Y_k - and after some algebraic manipulation, we get the Favre (mass) averaged conservation equations of fluid flow:

Mass

$$\frac{\partial \bar{\rho}}{\partial t} + \frac{\partial}{\partial x_i}(\bar{\rho}\tilde{u}_i) = 0 \tag{2.15}$$

Momentum

$$\frac{\partial \bar{\rho}\tilde{u}_i}{\partial t} + \frac{\partial}{\partial x_j}\left(\bar{\rho}\tilde{u}_i\tilde{u}_j\right) + \frac{\partial \bar{p}}{\partial x_i} = \left[\mu\left(\frac{\partial \tilde{u}_i}{\partial x_j} + \frac{\partial \tilde{u}_j}{\partial x_i}\right) - \frac{2}{3}\mu\frac{\partial \tilde{u}_k}{\partial x_k}\delta_{ij} - \overline{\rho u_i'' u_j''}\right] + \bar{\rho} g_i \tag{2.16}$$

Chemical species

$$\frac{\partial\left(\bar{\rho}\widetilde{Y_k}\right)}{\partial t} + \frac{\partial}{\partial x_i}\left(\bar{\rho}\tilde{u}_i\widetilde{Y_k}\right) = \overline{\dot{\omega}_k} + \frac{\partial}{\partial x_i}\left(\bar{\rho}D_k^M\frac{\partial \widetilde{Y_k}}{\partial x_i} - \overline{\rho u_i'' Y_k''}\right) \quad \text{for} \quad k = 1, N \tag{2.17}$$

Enthalpy

$$\frac{\partial\left(\bar{\rho}\widetilde{h_s}\right)}{\partial t} + \frac{\partial}{\partial x_i}\left(\bar{\rho}\tilde{u}_i\widetilde{h_s}\right) = \overline{\dot{\omega}_T} + \frac{\partial}{\partial x_i}\left(\bar{\rho}\alpha\frac{\partial \widetilde{h_s}}{\partial x_i} - \overline{\rho u_i'' h_s''}\right) + \overline{q_R'''} \tag{2.18}$$

The averaged equations yield a closure problem as new unknowns arise from the averaging process. The extra are the Reynolds stresses terms, in the momentum equation, and turbulent convective fluxes of the corresponding scalar quantity. To close the preceding system with the extra unresolved terms, it is required an appropriate turbulence model. Moreover, due to the averaging process of the flow equations, the solution will also be an averaged field.

2.3.2 Turbulence Models

Standard $k-\varepsilon$ Turbulence Model

According to the Boussinesq hypothesis (Chapter 5 in Pope, 2000), the Reynolds stresses tensor, $\overline{\overline{\rho u_i'' u_j''}}$, are proportional to the stress-rate-of-strain of a Newtonian fluid, following the relation below:

$$\overline{\overline{\rho u_i'' u_j''}} = \frac{2}{3}\bar{\rho}k\delta_{ij} - \mu_t\left(\frac{\partial \tilde{u}_i}{\partial x_j} + \frac{\partial \tilde{u}_j}{\partial x_i} - \frac{2}{3}\delta_{ij}\frac{\partial \tilde{u}_k}{\partial x_k}\right) \tag{2.19}$$

where, k is the turbulent kinetic energy defined as $k = \frac{1}{2}\overline{u_i'' u_j''}$, δ_{ij} is the Kronecker symbol and μ_t is the turbulent dynamic viscosity or the eddy viscosity. The turbulent fluxes of species and enthalpy can be closed with a gradient-diffusion hypothesis with the relations:

$$\overline{\overline{\rho u_i'' Y_k''}} = -\frac{\mu_t}{Sc_{t,k}}\frac{\partial \widetilde{Y_k}}{\partial x_i} \tag{2.20}$$

$$\overline{\overline{\rho u_i'' h_s''}} = -\frac{\mu_t}{Pr_t}\frac{\partial \widetilde{h_s}}{\partial x_i} \tag{2.21}$$

where, $Sc_{t,k}$ and Pr_t are the turbulent Schmidt number and the turbulent Prandtl number, accordingly.

Jones and Launder (1972) devised the standard $k-\varepsilon$ model, in which they define the turbulent kinematic viscosity, as well as, the transport equations for turbulent kinetic energy and turbulent kinetic energy dissipation rate, ε:

$$\mu_t = C_\mu \bar{\rho}\frac{k^2}{\varepsilon} \tag{2.22}$$

$$\frac{\partial}{\partial t}(\bar{\rho}k) + \frac{\partial}{\partial x_i}(\bar{\rho}\tilde{u}_i k) = \frac{\partial}{\partial x_i}\left[\left(\mu + \frac{\mu_T}{\sigma_k}\right)\frac{\partial k}{\partial x_i}\right] + \mathcal{P} + \mathcal{J} - \bar{\rho}\varepsilon \tag{2.23}$$

$$\frac{\partial}{\partial t}(\bar{\rho}\varepsilon) + \frac{\partial}{\partial x_i}(\bar{\rho}\tilde{u}_i \varepsilon) = \frac{\partial}{\partial x_i}\left[\left(\mu + \frac{\mu_T}{\sigma_\varepsilon}\right)\frac{\partial \varepsilon}{\partial x_i}\right] + C_{\varepsilon 1}\frac{\varepsilon}{k}(\mathcal{P} + C_{\varepsilon 3}\mathcal{J}) - C_{\varepsilon 2}\bar{\rho}\frac{\varepsilon^2}{k} \tag{2.24}$$

where $\mathcal{J}$ is the turbulent kinetic energy production terms due to buoyancy effects, which are neglected in the present numerical model. The turbulent kinetic energy production tensor due to the mean velocity gradients, $\mathcal{P}$, is given by

$$\mathcal{P} = -\overline{\rho u_i'' u_j''}\frac{\partial \tilde{u}_i}{\partial x_j} \tag{2.25}$$

The standard values for the model constants are (Launder and Sharma 1974)

$$C_\mu = 0.09; \quad C_{\varepsilon 1} = 1.44; \quad C_{\varepsilon 2} = 1.92; \quad \sigma_k = 1.0; \quad \sigma_\varepsilon = 1.3. \tag{2.26}$$

Reynolds Stress Transport Model (RSTM)

The $k-\varepsilon$ model models, in the absent of strain rate, calculate an isotropic turbulence field, whereas practical flows tend to be rather anisotropic and, for this reason, such models are very dissipative and inaccurate. On the other hand, the Reynolds-stress transport model is a second-order model and includes in its formulation the effects of streamline curvature, sudden changes in strain rate and secondary motions of the flow. Thus, the RSTM has more potential to capture the anisotropic turbulent stresses inside a combustor with enhanced mixing mechanisms such as the one addressed in this text.

The RSTM is based on the exact Reynolds-stresses transport equation, solving for each component of the Reynolds-stresses, $\tau_{ij} \equiv -\overline{u_i'' u_j''}$. The Boussinesq turbulence-viscosity assumption is no longer valid for this model. The model equations devised by Launder, Reece and Rodi (1975), the most used and revised second-order closure model, are presented below and were used in this work.

The transport equation of the Reynolds-stresses is given by:

$$\begin{aligned}\bar{\rho}\frac{\partial \tau_{ij}}{\partial t} + \bar{\rho}\widetilde{u_k}\frac{\partial \tau_{ij}}{\partial x_k} &\\ = \bar{\rho}\mathcal{P}_{ij} - \frac{2}{3}\bar{\rho}\varepsilon\delta_{ij} + \bar{\rho}\Pi_{ij} &\\ - C_s\frac{\partial}{\partial x_k}\left[\frac{\bar{\rho}k}{\varepsilon}\left(\tau_{im}\frac{\partial \tau_{jk}}{\partial x_m} + \tau_{jm}\frac{\partial \tau_{ik}}{\partial x_m} + \tau_{km}\frac{\partial \tau_{ij}}{\partial x_m}\right)\right]&\end{aligned} \tag{2.27}$$

and the energy dissipation rate transport equation takes the following form:

$$\bar{\rho}\frac{\partial \varepsilon}{\partial t} + \bar{\rho}\widetilde{u_k}\frac{\partial \varepsilon}{\partial x_k} = C_{1\varepsilon}\frac{\bar{\rho}\varepsilon}{k}\tau_{ij}\frac{\partial \tilde{u}_i}{\partial x_j} - C_{2\varepsilon}\frac{\bar{\rho}\varepsilon^2}{k} - C_\varepsilon\frac{\partial}{\partial x_j}\left(\frac{\bar{\rho}k}{\varepsilon}\tau_{km}\frac{\partial \varepsilon}{\partial x_m}\right) \tag{2.28}$$

The tensor Π_{ij} is the Pressure-Strain correlation and it can be expanded as follows:

$$\Pi_{ij} = C_1 \frac{\varepsilon}{k}\left(\tau_{ij} + \frac{2}{3}k\delta_{ij}\right) - \hat{\alpha}\left(\mathcal{P}_{ij} - \frac{2}{3}\mathcal{P}\delta_{ij}\right) - \hat{\beta}\left(\mathcal{D}_{ij} - \frac{2}{3}\mathcal{P}\delta_{ij}\right) - \hat{\gamma}k\left(S_{ij} - \frac{1}{3}S_{kk}\delta_{ij}\right) + \left[0.125\frac{\varepsilon}{k}\left(\tau_{ij} + \frac{2}{3}k\delta_{ij}\right) - 0.015\left(\mathcal{P}_{ij} - \mathcal{D}_{ij}\right)\right]\frac{k^{3/2}}{\varepsilon\, n} \quad (2.29)$$

where

$$\mathcal{P}_{ij} = \tau_{im}\frac{\partial \tilde{u}_j}{\partial x_m} + \tau_{jm}\frac{\partial \tilde{u}_i}{\partial x_m} \quad (2.30)$$

$$\mathcal{D}_{ij} = \tau_{im}\frac{\partial \tilde{u}_m}{\partial x_j} + \tau_{jm}\frac{\partial \tilde{u}_m}{\partial x_i} \quad (2.31)$$

$$S_{ij} = \frac{1}{2}\left(\frac{\partial \tilde{u}_i}{\partial x_j} + \frac{\partial \tilde{u}_j}{\partial x_i}\right) \quad (2.32)$$

$$\mathcal{P} = \frac{1}{2}\mathcal{P}_{kk} \quad (2.33)$$

The first term in the Pressure-Strain correlation is called the slow pressure-strain term or return-to-isotropy term, as postulated by Rotta (1951). The following three terms constitute the rapid pressure-strain terms and the last is the pressure-echo effect or the wall-reflection effect term, proposed by Gibson and Launder (1978), where n is the normal distance to the wall. The remaining unclosed terms in the previous equations are model constants and they are listed as follows:

$$\begin{array}{lll} \hat{\alpha} = (8 + C_2)/11; & \hat{\beta} = (8C_2 - 2)/11 & \hat{\gamma} = (60C_2 - 4)/55 \\ C_1 = 1.8 & C_2 = 0.60 & C_s = 0.11 \\ C_\varepsilon = 0.18 & C_{1\varepsilon} = 1.44 & C_{2\varepsilon} = 1.92 \end{array} \quad (2.34)$$

2.3.3 Conservation equations for turbulent flows

Using the relations presented for turbulent flows, equations (2.16), (2.17) and (2.18) can be rewritten by replacing the Reynolds stresses and the turbulent fluxes terms by the correspondent model relations as follows:

Momentum equation

$$\frac{\partial \bar{\rho}\tilde{u}_i}{\partial t} + \frac{\partial}{\partial x_j}\left(\bar{\rho}\tilde{u}_i\tilde{u}_j\right) + \frac{\partial \bar{p}}{\partial x_i} = \left[\mu_{eff}\left(\frac{\partial \tilde{u}_i}{\partial x_j} + \frac{\partial \tilde{u}_j}{\partial x_i}\right) - \frac{2}{3}\left(\mu_{eff}\frac{\partial \tilde{u}_k}{\partial x_k} + \bar{\rho}k\right)\delta_{ij}\right] + \bar{\rho}g_i \quad (2.35)$$

where $\mu_{eff} = \mu + \mu_t$ is the effective dynamic viscosity.

Mass conservation equation of species

$$\frac{\partial\left(\bar{\rho}\widetilde{Y_k}\right)}{\partial t} + \frac{\partial}{\partial x_i}\left(\bar{\rho}\tilde{u}_i\widetilde{Y_k}\right) = \overline{\dot{\omega}_k} + \frac{\partial}{\partial x_i}\left(D^M_{eff,k}\frac{\partial\widetilde{Y_k}}{\partial x_i}\right) \qquad \text{for} \quad k = 1, N \qquad (2.36)$$

where $D^M_{eff,k}$ is the effective mass diffusion coefficient given by:

$$D^M_{eff,k} = \bar{\rho}D^M_k + \frac{\mu_t}{Sc_{t,k}} \qquad (2.37)$$

In highly turbulent driven flows, $\bar{\rho}D^M_k$ is much smaller than the turbulent diffusivity term ($\mu_t/Sc_{t,k}$) and can be simply neglected (Poinsot and Veynante, 2001; Parente *et al.,* 2008). Therefore, equation (2.36) is rewritten as:

$$\frac{\partial\left(\bar{\rho}\widetilde{Y_k}\right)}{\partial t} + \frac{\partial}{\partial x_i}\left(\bar{\rho}\tilde{u}_i\widetilde{Y_k}\right) = \overline{\dot{\omega}_k} + \frac{\partial}{\partial x_i}\left(\frac{\mu_t}{Sc_{t,k}}\frac{\partial\widetilde{Y_k}}{\partial x_i}\right) \qquad \text{for} \quad k = 1, N \qquad (2.38)$$

and $Sc_{t,k} = 1$ for all species.

Enthalpy equation

$$\frac{\partial\left(\bar{\rho}\widetilde{h_s}\right)}{\partial t} + \frac{\partial}{\partial x_i}\left(\bar{\rho}\tilde{u}_i\widetilde{h_s}\right) = \overline{\dot{\omega}_T} + \frac{\partial}{\partial x_i}\left(\alpha_{eff}\frac{\partial\widetilde{h_s}}{\partial x_i}\right) + \overline{q'''_R} \qquad (2.39)$$

where α_{eff} is the effective thermal diffusion coefficient given by:

$$\alpha_{eff} = \frac{\lambda}{c_p} + \frac{\mu_t}{Pr_t} \qquad (2.40)$$

2.4 Turbulence/Chemistry Interaction Model

The unclosed consumption/production of species term in the averaged species equation (2.17), $\overline{\dot{\omega}_k}$, was closed with the Partially Stirred Reactor model (PaSR) devised by Karlsson (1995). The PaSR model is the turbulence/chemistry interaction model implemented in OpenFOAM®. Contrary to the *flamelets* approach, the concept of the PaSR ignores the sub-grid laminar structure of the turbulent flame and, considering that real flames are much thinner than any computational cell in the domain, it assumes that the entire cell is a perfect reactor (Nordin, 2001). This model was first introduced to study turbulent diesel spray combustion, as an extension to the Eddy Dissipation Model (EDM) by Magnussen and

Hjertager (1976). In principle, the PaSR model is also similar to the successful EDC model, despite the mathematical formalism being different.

The following list describes the fundamental principles of the PaSR model and how it processes the reaction rates at each time iteration (Nordin, 2001):

A. the PaSR model considers that any computational cell is divided into a reacting part and a non-reacting part. The size of the reacting part is at sub-grid level, since the sum of both reacting and non-reacting parts is the actual cell (smallest spatial unit), and, conversely, is unknown;
B. the reacting part is also treated as a perfectly stirred reactor (PSR) where the all species are homogeneously mixed;
C. at the beginning of the time iteration, t_0, the averaged concentration in the cell and entering the cell is c_0 and is known from the previous iteration.
D. the mixture inside the reacting part reacts completely and the new concentration inside this part is c. This concentration is unknown at any time iteration and the duration of this reaction is equal to the numerical time step of the current iteration, τ;
E. when the reaction is complete, the species in the reacting part and non-reacting part are assumed to mix due turbulence and the time of this procedure is dictated by the mixing time τ_{mix};
F. at the end of the time step, t_1, the averaged concentration in the cell and leaving the cell is c_1. This is the unknown the model solves for.

The following equations describe the process mathematically:

$$c_1 = \kappa^* c + (1 - \kappa^*) c_0 \tag{2.41}$$

$$\kappa^* = \frac{\tau}{\tau + \tau_{mix}} \tag{2.42}$$

where κ^* is the reactive fraction of the reactor cell. As seen in equation (2.42), the relative size of each part of the reactor is dictated by a relation between the residence time (also the numerical time step, τ) and the turbulent mixing time (or turbulent timescale), τ_{mix}. In fact, if the residence time is much larger than the turbulent mixing time, κ^* will be close to unit and the reactor will be most entirely reactive. The relation between the unclosed consumption/production rate of species k, $\overline{\dot{\omega}_k}$, and the laminar rate consumption/production of species is given by:

$$\overline{\dot{\omega}_k} = \frac{c_1^k - c_0^k}{\tau} = \frac{\tau_c}{\tau_c + \tau_{mix}} \dot{\omega}_k = \kappa \dot{\omega}_k \tag{2.43}$$

where τ_c is the chemical timescale and $\dot{\omega}_k$ is given by equation (2.10). The turbulent mixing time is determined using the turbulent quantities as follows (Peng, 2008):

$$\tau_{mix} = C_{mix} \sqrt{\frac{\mu_{eff}}{\bar{\rho}\varepsilon}} \qquad \text{with } C_{mix} = 0.03 \tag{2.44}$$

The chemical timescale is taken from the characteristic time of the chemical reaction system (2.11) consisted of $N \times M$ Ordinary Differential Equations (ODEs).

2.5 Radiation Models

2.5.1 Discrete Ordinates Method

The differential radiative transfer equation in a non-scattering grey medium is, according to Modest (2003):

$$\frac{dI(\vec{s})}{ds} = \kappa_m[-I(\vec{s}) + I_b] \tag{2.45}$$

where $I(\vec{s})$ is the radiation intensity in the $\vec{s}$ direction, I_b is the blackbody radiation intensity and κ_m is the medium absorption coefficient. For a diffusely emitting and diffusely reflecting grey surface, the boundary condition for equation (2.45) is:

$$I_w(\vec{s}) = \varepsilon_w I_{bw} + \frac{\rho_w}{\pi} \int_{\vec{n}.\vec{s}'} I(\vec{s}') \, |\vec{n}.\vec{s}'| \, d\Omega' \tag{2.46}$$

where $I_w(\vec{s})$ is the radiation intensity leaving the surface, $I(\vec{s}')$ is the incident radiation in the $\vec{s}'$ incoming direction and confined to the solid angle $d\Omega'$, I_{bw} is the blackbody radiation intensity at surface temperature, $\vec{n}$ is the surface's normal direction and ε_w and ρ_w represent the surface emissivity and reflectivity, accordingly.

To solve the previous equations, the Discrete Ordinates Method (DOM), proposed by Fiveland (1984), was applied. The method discretizes the solid angle into *N* distinct directions and formulates a new differential equation for each one:

$$\frac{dI^n}{ds} = \kappa_m[-I^n + I_b] \tag{2.47}$$

and the corresponding boundary condition:

$$I_w^n = \varepsilon_w I_{bw} + \frac{\rho_w}{\pi} \sum_j I^j \left|\vec{n}.\vec{s}_j\right| w_j \qquad , \vec{n}.\vec{s}_n > 0 \tag{2.48}$$

where n is the direction index. The integrals over the solid angles are approximated by a numerical quadrature of *S* order and w_j is the quadrature weight for direction *j*.

The radiative heat source term on enthalpy equation (2.18) is evaluated as

$$\overline{\overline{q_R'''}} = \kappa_m(4\sigma T^4 + G) \tag{2.49}$$

in which T is the medium temperature, σ is the Stefan-Boltzmann constant and G is the incident irradiation given by

$$G = \int_{4\pi} I \, d\Omega \approx \sum_{j=1}^{N} w_j I^n \tag{2.50}$$

The properties of the medium were determined assuming a grey gases mixture and a transparent gas. The total emissivity of the mixture is given by the correlation

$$\varepsilon_m = \sum_{i=1}^{I} a_{\varepsilon,i}(T)\left(1 - e^{-k_i P_i s}\right) \tag{2.51}$$

where $a_{\varepsilon,j}$ is the radiative energy fraction emitted by a black body in the range of wavelengths, in which the spectral absorption coefficient of the mixture is similar to the absorption coefficient of gas *i*, P_i is the partial pressure of gas *i*, k_i is a model parameter and *s* is the mean path length. As common practice in combustion calculation, only CO_2 and H_2O were considered as absorbent gases and the values of $a_{\varepsilon,i}$ and k_i published in Coppalle and Vervish (1983) and Smith (1982) were used.

2.5.2 The Method of Spherical Harmonics. The P_1-Approximation.

The P_1-approximation is the most popular spherical harmonics method for arbitrary geometries and is a particular form of the more generic spherical harmonics method. It

reduces the integral equation of radiative heat transfer to a simple partial differential equation. The radiative intensity field $I(r,\vec{s})$ for the P_1-approximation is obtained when the Fourier series describing the spherical harmonics method is truncated beyond $l = 1$, that is (Modest, 2003):

$$I(r,\vec{s}) = I_0^0 Y_0^0 + I_1^{-1} Y_1^{-1} + I_1^0 Y_1^0 + I_1^1 Y_1^1 \tag{2.52}$$

where, Y_l^m are the *spherical harmonics*. Replacing the spherical harmonics and the associated Legendre polynomials in equation (2.52), it is possible to show that the radiative intensity field can be rewritten in terms of the incident radiation, $G(r)$, and the radiative heat flux, $\vec{q}(r)$, yielding (Modest, Radiative Heat Transfer, 2003):

$$I(r,\vec{s}) = \frac{1}{4\pi}[G(r) + 3.\vec{q}(r)\cdot\vec{s}] \tag{2.53}$$

The preceding equation is the starting point to derive the physical significance of the P_1-approximation method, as done by Modest (1976), who considered radiation as a "photon gas" with momentum and energy associated and described radiative intensity field based on quantum statistics principles. His work showed that equation (2.53) holds only for points located at a large optical distance ($\tau_{op} > 3$) away from any sharp temperature gradients or any other strong thermodynamic perturbation. Finally, by applying equation (2.53) into the general equation of radiative heat transfer and assuming linear-anisotropic scattering, the governing equations for the radiative transfer for the P_1-approximation method are obtained:

$$\nabla_\tau \cdot \vec{q} = (1-\omega)(4\pi I_b - G) \tag{2.54}$$

$$\nabla_\tau G = -(3 - A_1\omega)\vec{q} \tag{2.55}$$

where ∇_τ is the divergent operator written for the space coordinates nondimensionalized using the extinction coefficient. Then, equation (2.49) is used to compute the radiative heat source, q_R''', in the energy equation. The Marshak's boundary condition (Marshak, 1947) was applied to close the radiative transfer equations at the boundaries of the numerical domain and the radiative properties of the medium were determined with the same method used with the DOM.

Even thought the P_1-approximation method is known to yield imprecise results for optically thin media, it has reasonable accuracy for large optical distances ($\tau_{op} > 3$) and, thus, is suitable for combustion.

CHAPTER 3

NUMERICAL RESULTS AND DISCUSSION

The following chapter presents the computational results obtained with OpenFOAM® for the investigation of the FLOXCOM® combustor prototype. The first set of results cover the non-reacting flow field analysis inside the combustor. Here, a grid dependence analysis was carried out with three meshes discretizing the combustor in three different ways. Also, the effects of the standard $k-\varepsilon$ model and the second-order RSTM turbulence model on the numerical solution were scrutinized. The results were compared with experimental data published in Melo (2006).

The second set of results consists of a benchmark test of the PaSR combustion model implemented in OpenFOAM®. The simulation comprised a lifted, non-premixed turbulent methane flame, studied experimentally and numerically by Mahmud *et al.* (2007). Experimental data including temperature profiles, flame shape and lift-off height were compared with the results obtained. The test was carried out with an axisymmetric, structured mesh, the standard $k-\varepsilon$ model turbulence model and the method of discrete ordinates to resolve the radiative fluxes. The influence of the level of detail of the chemical mechanism employed with the combustion model was also investigated with the simplified Westbrook and Dryer 2-step mechanism, the skeletal Smooke mechanism and the detailed GRI-2.11 reaction mechanism.

We end the present study with a simulation of the FLOXCOM® combustor prototype with chemical reactions enabled. The temperature and species distributions were resolved and compared against the experimental data presented in Melo (2006). Methane was used as fuel and the chemical mechanism considered was the skeletal Smooke mechanism. Turbulence was modeled with the RSTM turbulence model and the radiative fluxes were determined with the P_1-approximation method.

3.1 Non-reacting flow analysis of the FLOXCOM® Combustor

This section reports the results of the non-reacting computational analysis carried out on the FLOXCOM® combustor prototype. The purposes of this investigation are to validate the numerical results obtained with the experimental data available and get a better insight on the mechanisms governing the flow field inside the combustor, namely the mixing processes and the recirculation motions. We start the section by describing the numerical set-up: geometry of the combustor, operating conditions, numerical domain, and initial and boundary conditions.

3.1.1 Numerical set-up

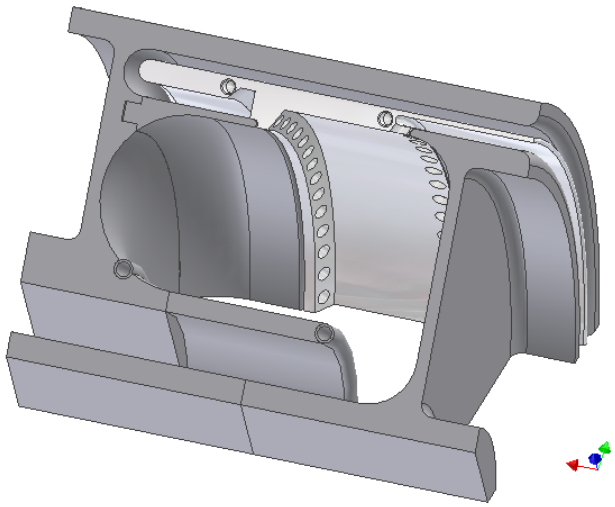

Figure 4 – CAD representation of the FLOXCOM® combustor prototype (Melo, 2006).

Geometry

The FLOXCOM® is a novel GT annular combustor concept with a very larger recirculation zone, designed to operate in flameless conditions. Even though there are several designs following the basis of the FLOXCOM® combustor, we focused this investigation on

the prototype studied by Melo (2006), in IST, shown in Figure 4. The prototype consists of a 60 degrees wedge-section of the total annular combustor. The longitudinal cross-section is sketched in Figure 5.

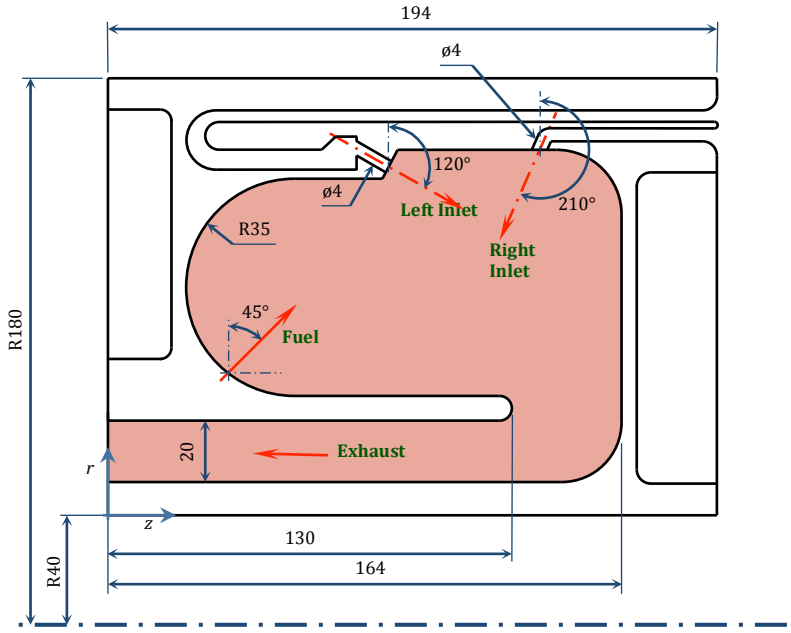

Figure 5 – Cross-section of the FLOXCOM® combustor prototype (Melo, 2006).

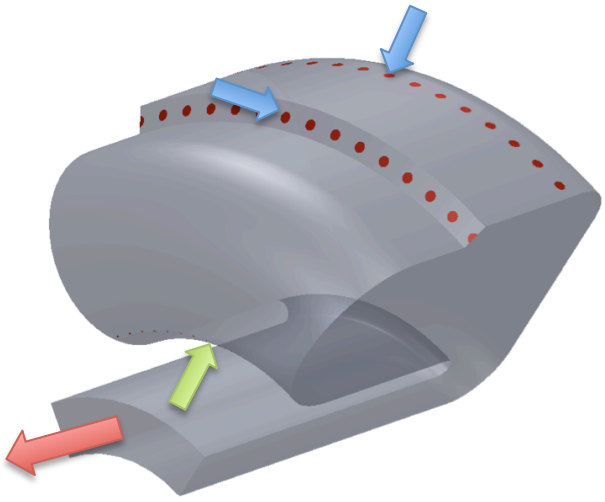

Figure 6 – Computational domain corresponding to the interior volume of the FLOXCOM® combustor with flow schematics: blue arrows represent the combustion air intake; the green arrow represents fuel intake; and the red arrow represents the outflowing exhaust gases.

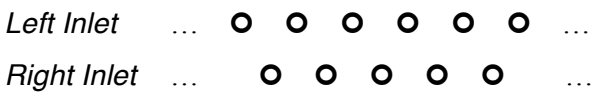

Figure 7 – Staggered arrangement of the air injection holes.

The colored area in Figure 5 highlights the combustion zone, dilution zone and exhaust, which, combined, correspond to the numerical domain considered for the analysis and shown in Figure 6. Pre-heated air enters the combustion chamber through the Right inlet, with 14 injection holes at 210º relatively to the radial direction, and through the Left inlet, with 14 injection holes at 120º relatively to the radial direction. The air injection holes have 4 mm diameter and are arranged in a staggered pattern, uniformly spaced, as illustrated in Figure 7.

The fuel is injected at 45º from the radial direction through 15 injection holes evenly distributed in the tangential direction, with an internal diameter of 2 mm. The dilution zone and the exhaust opening are located in the inner radius of the combustor, as illustrated in Figure 5. Notice that the air mass flux through each entrance, marked with the blue arrows at the top of Figure 6, is equal, being exactly half of the total airflow reaching the combustor. This allows us to disregard the flow inside the channels upstream of the combustor from the numerical domain.

Operating Conditions

In Melo (2006), several sets of operating conditions were tested. For the interest of this investigation, only the configuration leading to the flameless combustion regime with ultra-low levels of NO_x and higher overall combustion efficiency was selected. Table 1 summarizes the operating conditions chosen for the analysis:

Total airflow	1.7 m^3/s @ atmospheric pressure and pre-heated to 425 K
Fuel	Methane (CH4) @ 293 K
Equivalent ratio	0.28

Table 1 – Operating conditions (Melo, 2006).

Grid

To spare some computational effort, one can take advantage of the axisymmetric domain and reduce the computational domain to a smaller section of the original 60-degrees combustor. For this effect, periodic boundary conditions must be implemented at each bounding faces (Figure 8) to virtually represent the flow that is not numerically represented

and keep the integrity of the numerical domain relatively to the original 60-degrees domain. In order to evaluate the validity of this abbreviation of the domain, three sections with 60/14-degrees (section A), 180/14-degrees (section B) and 30-degrees (section C) were considered, corresponding to $1/14^{th}$, $3/14^{th}$ and 1/2 of the original 60-degrees section (Figure 9). Accordingly, on the Left and Right inlets, section A has one inlet hole, section B has three inlet holes and section C has seven inlet holes, with the number of fuel injector holes following the same distribution.

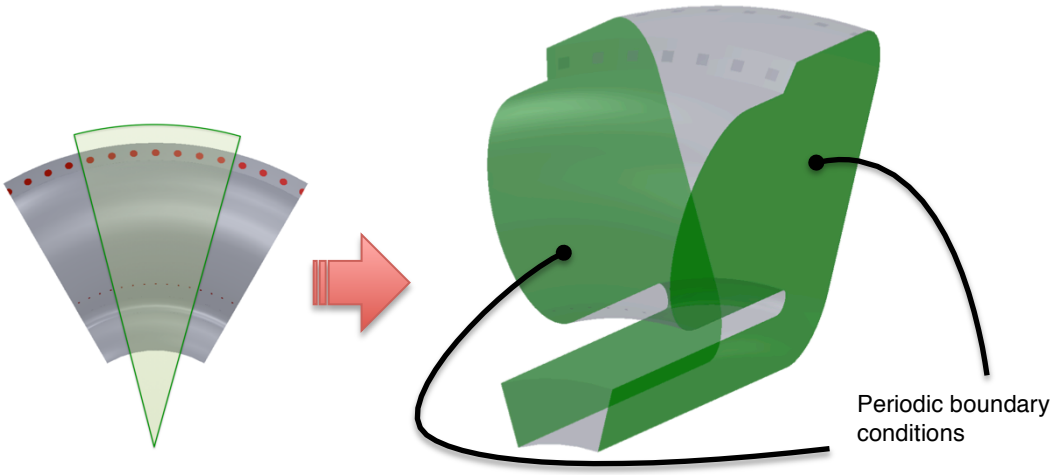

Figure 8 – Reduced computational domain with periodic boundary conditions implemented on the bounding faces (highlighted in green). The green sector at the left represents the slice of the original 60-degrees combustor represented by computational domain on the right.

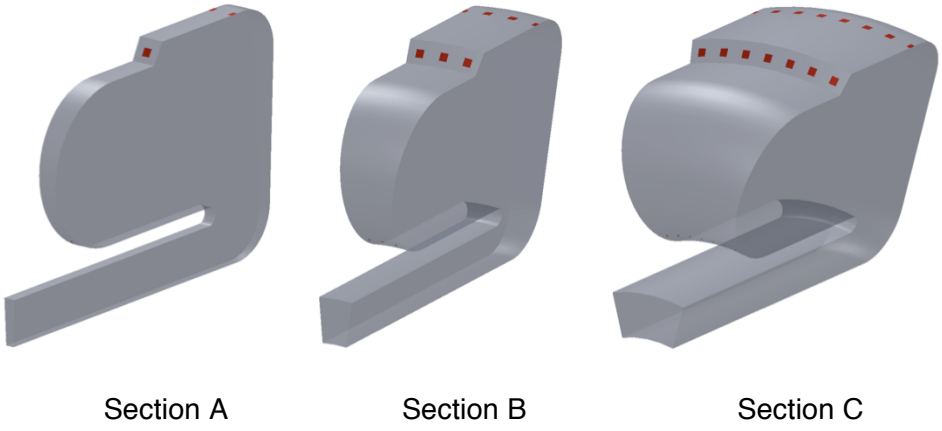

Figure 9 – The three reduced computational domains used for the analysis of the FLOXCOM® combustor.

Unstructured grids were used for all three sections. Even though there is some loss in accuracy with the unstructured grid, fitting a structured grid in such complex geometry is very

cumbersome and time consuming. On the other hand, with the unstructured grid, we easily fit an orthogonal grid layer near the wall and around the recirculation zone, as highlighted in Figure 10, so that the flow stays aligned with the grid and the high gradients near the wall are better resolved. The grids consist of hexahedron elements only. The mesh of section A has 39508 cells, section B has 109384 cells and section C has 253878. The cell density was made similar for every section. Because the elements used are hexahedron, for convenience, the section of both air and fuel inlets was changed to a square, with an equivalent area as the original circular inlet. By taking this assumption, it is expected that, due to viscous effects, the differences in secondary flow characteristics of the square jet and the round jets are rapidly attenuated and are of much smaller order of the flow patterns of interested for this work. All the grids were set up with the Gambit® software package and then exported to OpenFOAM®.

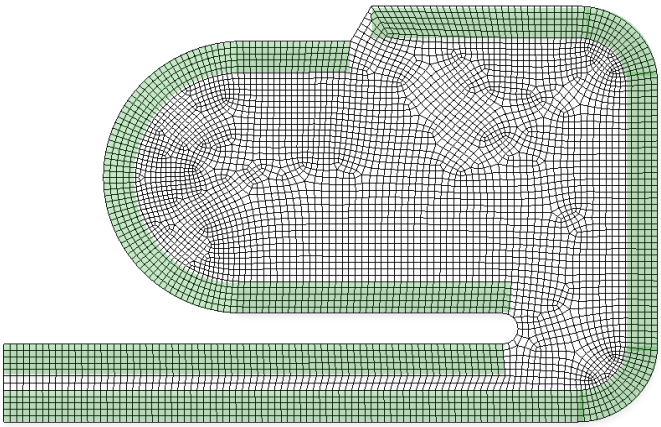

Figure 10 – Cross-section grid layout of the FLOXCOM® combustor prototype. The orthogonal grid layer near the wall highlighted in green.

Numerical procedure

An implicit pressure-correction algorithm, the PISO algorithm, was used to solve the unsteady flow field. The flow field equations were discretized with the MUSCL scheme, except for the radiative heat transfer equation that was discretized with a linear upwind differencing scheme. The second-order MUSCL convective scheme is ideal to resolve the strong gradients generated by the highly turbulent flow, not only near the combustor walls, but mainly in the region where the inlet combustion air jets and recirculating products interact. Furthermore, as the flow is mostly aligned with the grid in the recirculation zone, less discretization errors are expected.

The convergence criteria were based on the residuals of the equations being solved. For the simulation obtained with the standard $k-\varepsilon$ model, the solution was considered converged when continuity, momentum and turbulent kinetic energy equations residuals were lower than 1×10^{-5}. It was found that as soon the residuals met this criterion, there were no tangible changes in the solution. For the simulations with the RSTM, because of the unsteadiness of the Reynolds-stress transport equation residuals, the convergence criterion was additionally based on the total mass-flux imbalance of the computational domain, such that convergence was attained when the mass-flux imbalance was lower than 10^{-7}, and the former criteria were also matched. All simulations in this work were carried out until the solution field converged to assure the best possible quality of the numerical results.

The maximum courant number was set to the unity, limiting the time-step to $\approx 1.4\times 10^{-5}$. The under-relaxation factors were set to 0.8 for all quantities for the run with the standard $k-\varepsilon$ model turbulence model and, for the simulation with the RSTM model, the under-relaxation factors for velocity, pressure and Reynolds-stresses tensor were set to 0.4, in order to smooth the strong unsteadiness. The simulations with the standard $k-\varepsilon$ turbulence model were run in a 8-core Xeon® "Nehalem" machine, taking less than half day to completion, while the simulations with the RSTM turbulence model took about one day to achieve convergence in a 16-cores cluster set-up available in the Amazon Elastic Compute Cloud (Amazon EC2) provided by Amazon Web Services™.

Initial and boundary conditions

The boundary conditions were determined based on the operating conditions listed on Table 1. Because the velocity profile at the inlets was unknown, the mass flux was fixed at all inlets. Also, inlet temperature is fixed for all inlets. At the outlet, pressure is fixed and set to the ambient pressure. The inlet air was approximated as an ideal mixture composed by 21% of O_2 and 79% N_2 in volume fraction. The initial turbulent fields were estimated considering a turbulent intensity of 10% and a length scale of 1/100th of the recirculation region diameter. The initial solution for the simulations with the RSTM turbulence model was taken from the solution field obtained with the standard $k-\varepsilon$ turbulence model.

3.1.2 Solution dependency on the grid and turbulence models

This section highlights the effects of the axisymmetric domain abbreviation with periodic boundary conditions and the effect of both the standard $k-\varepsilon$ model and RSTM turbulence models on the numerical solution.

Figure 12 shows the plotted results of the axial, radial and tangential velocity profiles obtained for sections A, B and C with both turbulence models at the center of the recirculation region and in the combustor symmetry plane (z = 0.09 m and θ = 0, see Figure 11). The standard $k-\varepsilon$ turbulence model solution is represented with the dashed colored lines while the solid colored lines represent the RSTM model solution. The black diamonds indicate the experimental data reported in Melo (2006). It is relevant to remind at this stage that since one is dealing with a URANS turbulence model, the numerical solution is a mean (or averaged) solution.

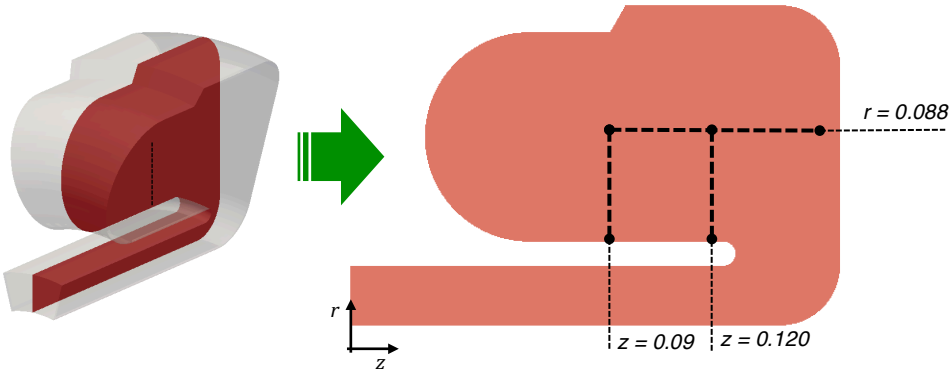

Figure 11 – Samples locations of the results plotted on Figures 12, 13 and 14. Units in meters.

In general, the results show reasonable agreement with the experimental results either with the standard $k-\varepsilon$ turbulence model or with the RSTM model at the considered location. Also, no significant differences are observed relatively to the solutions obtained for the three different sections. Even though there were no measurements available for the tangential velocity component at any location of the combustor, Melo (2006) verified, with LDA measurements in a slightly tilted plan from the mid-plane, that the tangential velocity component is of much lower order of magnitude than the axial and radial components. Thus, the predicted tangential velocity profile in Figure 12 is consistent with the latter experimental observation, yielding values not higher than 0.5 m/s.

Figure 13 reveals lower turbulence kinetic energy in the regions farther from the wall for all sections and for both turbulence models, relatively to the experimental data. Nevertheless, it should be noted that, in Melo (2006), the turbulent kinetic energy was projected assuming an estimated value for the tangential velocity fluctuation based on the measured axial and radial velocity fluctuations, as in equation (3.1). Thus, one should not rely completely on this information but rather see this data only as a reference for its order of magnitude.

$$k = \frac{1}{2}\left[u'^2 + v'^2 + \frac{1}{2}(u'^2 + v'^2)\right] \tag{3.1}$$

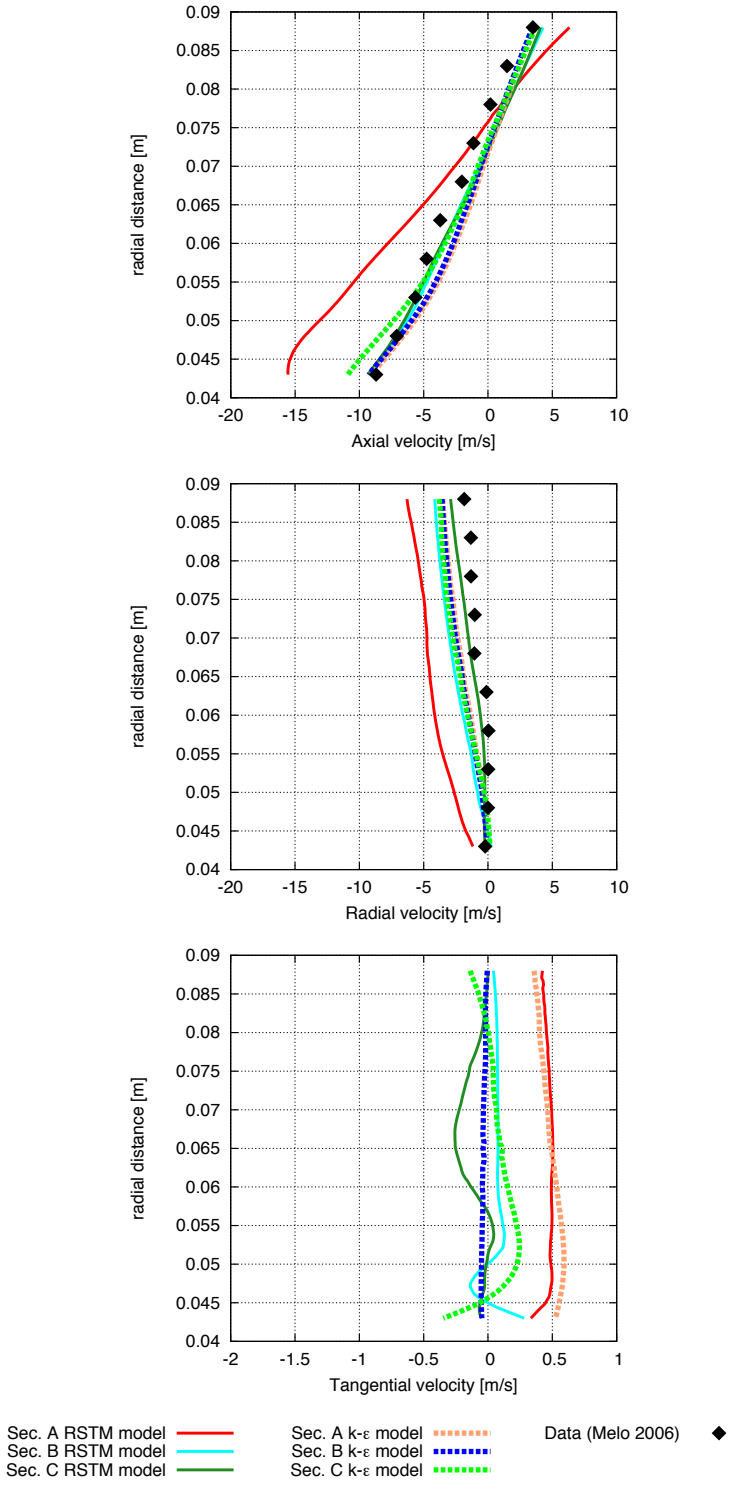

Figure 12 – Axial, radial and tangential velocity fields at the center of the recirculation region of sections A, B and C, obtained with the standard $k - \varepsilon$ and the RSTM turbulence models, with experimental data.

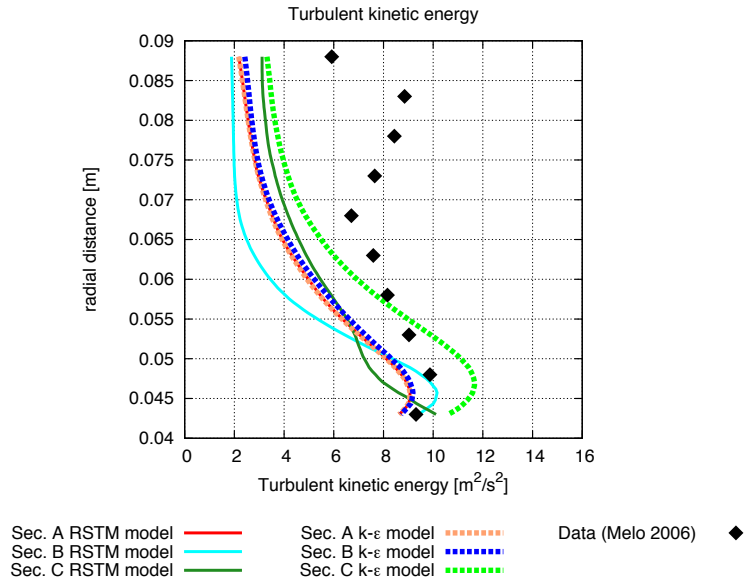

Figure 13 – Turbulent kinetic energy at the center of the recirculation region, with experimental data.

The velocity profiles predicted with the standard $k-\varepsilon$ turbulence model for the three different sections showed only minor differences, denoting that the abbreviation of the domain has little influence on the converged numerical solution for this model. On the other hand, with the RSTM model, the solution of Section A revealed relatively large deviation from the experimental results near the wall and, whilst the solution of Section C exhibited the best match with the experimental data of all numerical solutions, particularly for the radial velocity component, as verified in Figure 12. It is believed that this inconsistency is owned to the enhanced sensibility of the RSTM model to the flow. Unlike the standard $k-\varepsilon$ turbulence model, the second-order RSTM turbulence model has a transport equation for each Reynolds-stress component and, as a result, the final solution is more sensible to the secondary flow motions developing in the tangential direction.

Figure 14 displays the velocity distribution inside the FLOXCOM® combustor at other two different locations: z = 0.120 m and r = 0.088 m, as illustrated in Figure 11. As observed in Figure 14, the numerical solution over-estimates, in general, the velocity distribution in this area, although it reproduces the experimental data near the wall with reasonable accuracy. This suggests that both turbulence models are not able to capture the energy dissipation due to the viscous effects. On the other hand, it also suggests that the wall-interaction models included in the turbulence models are sufficient to solve the flow near the wall without further grid refinements.

In general, apart from the experimental data, the solutions obtained for all sections with either turbulence models were fairly similar, showing only minor discrepancies between each other. Thus, this indicates that the numerical solution is little influenced by the abbreviation of the numerical domain and, accordingly, one can infer that it is possible, to a certain extent, to take advantage of the axisymmetric geometry of the combustor to reduce the size of the computational domain using periodic boundary conditions, without losing the integrity of the numerical solution.

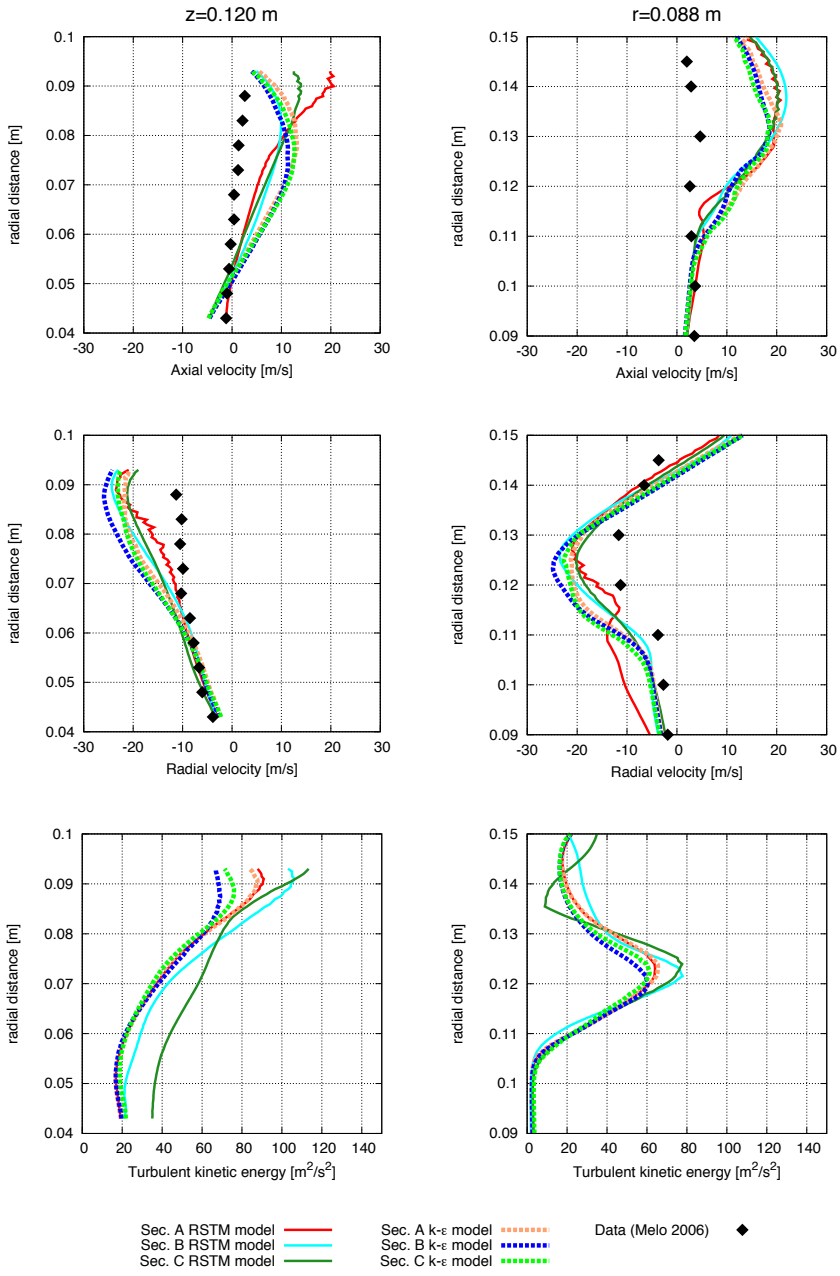

Figure 14 – Measured and predicted axial and radial velocity components distribution at locations z=0.120 and r=0.088.

3.1.3 Flow Field analysis

In this section, the non-reacting flow inside the FLOXCOM® combustor is analyzed, with emphasizes to the velocity fields and turbulence quantities. From this analysis, the goal is to get a better understanding on the flow mechanics controlling the mixing processes and driving the recirculation motion and the possible undesirable effects corrupting the aerodynamic efficiency of the combustor. This investigation is based on the numerical results obtained with section B, the RSTM turbulence model and the operating conditions listed in Table 1. The Reynolds number of the non-reacting flow at the specified operating conditions and based on the recirculation region diameter, D_R = 70 mm, is 22242, evidencing a strong turbulent flow. Figures 15 and 16 show the magnitude contours of the mean velocity field and the corresponding vector orientations at two different meridian planes: the central plane of the combustor (also the symmetry plane), cutting the Left inlet, and a second plane slightly tilted back around the combustor's revolution axis, cutting the Right inlet.

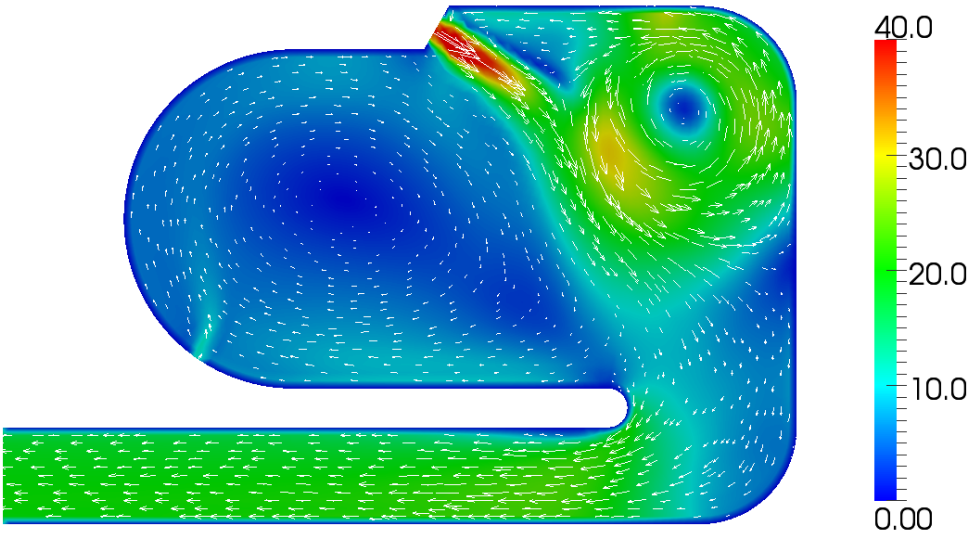

Figure 15 – Contour of the mean velocity field at the mid-meridian-plane, cutting the Left inlet. Units m/s.

Figures 15 and 16 highlight two recirculating flows: a primary recirculating flow occupying 60-70% of the combustor's volume (excluding the exhaust channel) and a smaller but stronger recirculating motion occupying about 15-20% of the combustor volume and located just downstream the Right inlet. The larger recirculating motion is the key region of the FLOXCOM® combustor concept and its purpose is to generate a homogeneous hot mixture of fresh combustion air and burnt products and hold stable flameless combustion. The smaller counter-clockwise flow motion is a parasite flow behavior, resulting from the

interaction between the Right inlet jets and the stagnant air on the right of the jets. In fact, this unwanted flow effect dissipates a considerable amount of the energy and momentum carried in by the jet and, as a result, the primary recirculating flow becomes weaker.

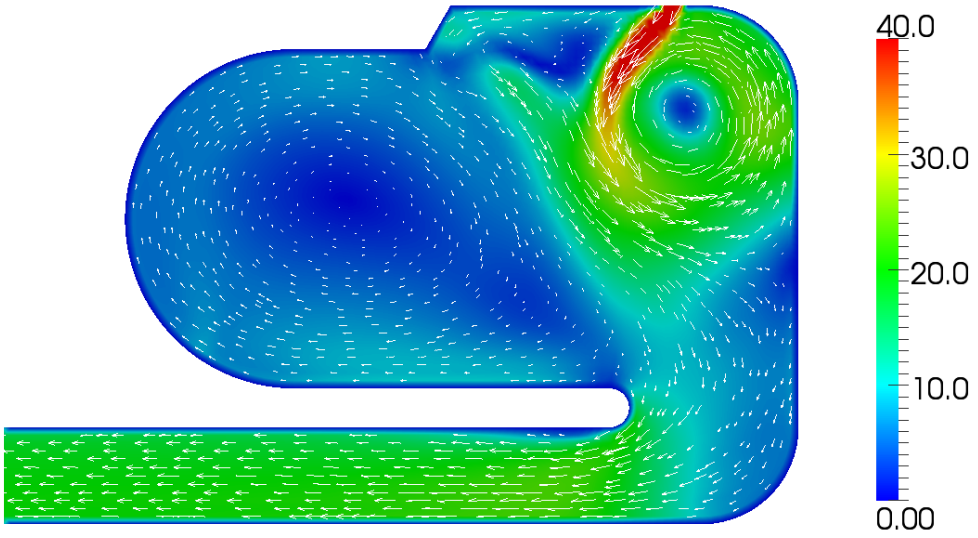

Figure 16 – Contour of the mean velocity field at the meridian-plane cutting the Right inlet. Units m/s.

The clockwise motion of the large recirculation region is controlled mainly by the Right inlet jets, as showed on Figure 16, "pushing" fresh combustion air towards that region. On the other hand, the Left inlet jets drags a portion of the recirculating air stream towards the exhaust channel while it also transfers some of its momentum to the recirculation motion, because of the viscous effects. Furthermore, the interaction between both the Left and Right inlet jets allows some fresh air to be directed straight to the dilution channel, as one can infer from the vector orientations of Figures 15 and 16. This stream is important to cool down the exhaust gases and homogenize the temperature profile at the outlet.

Figure 17 displays the turbulence kinetic energy contour at an intermediate meridian plane between both inlets and in the transverse plane A at $z = 120$ mm. As observed in Figure 17, a strong turbulent stream develops from the high-speed jets through the Left inlets. This turbulent flow is then transported downstream to the dilution zone and to the recirculation region. The strong fluctuations associated to the turbulent flow promote fast mass diffusion, which benefits the mixture between fresh air, combustion products and fuel and increases the contact area between fuel and oxidant, enhancing combustion efficiency. Thus, it is expected that turbulence at the entrance of the recirculation region and being transported inside the reaction zone will play an important role in the mixing rates and in the overall combustion efficiency. As seen on Figure 17, the Right inlet jets produce little

turbulent stresses as they develop towards the interaction zone, comparing with the Left side jets. A possible explanation has to do with the fact the parasite recirculating motion attached to the exit of these jets is dissipating most of its the kinetic energy and momentum, attenuating turbulent intensity. Further downstream, due to the dissipative viscous effects, the turbulent fluctuations lose their intensity as they penetrate more into the combustor, as observed in Figure 17. At the entrance of the exhaust channel, however, the turbulent kinetic energy levels are still significant. This turbulence is responsible for diluting the hot combustion products leaving the combustor with the dilution air, providing a proper temperature profile of the exhaust gases at the entrance of the turbine's first stage blades.

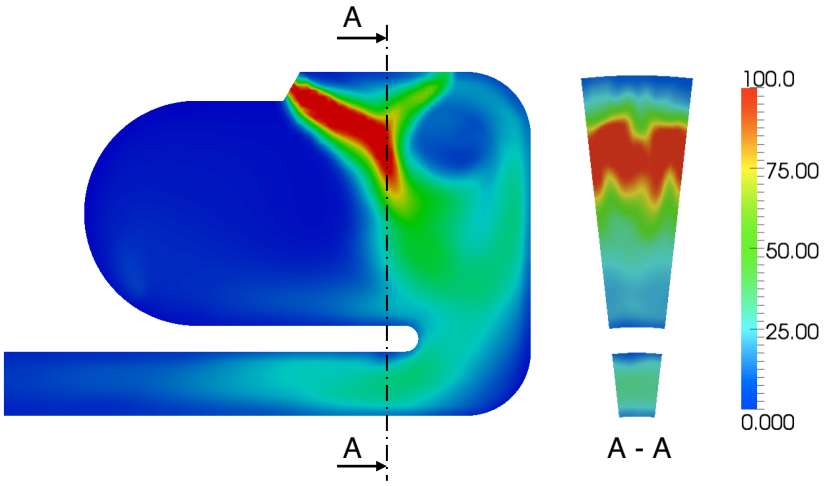

Figure 17 – Turbulent kinetic energy contours at an intermediate meridian plane between both inlets and in a transverse plane at $z = 120$ mm. Units m^2/s^2.

In summary, we could identify two recirculation motions in the non-reacting flow inside the combustor: the primary and large recirculation region, holding the reaction zone, and a parasite secondary motion attached to the exit of the Right inlet jets. This latter recirculating region does not contribute in any sense to the aerodynamics of the combustor. In fact, it acts as a momentum and energy sink to the Right inlet jets, that lose their strength to it, and inhibits the turbulence generation at the Right inlet jets. It was also found that the main source of turbulence in the flow are the Left inlet jets, which are also responsible for the transport of the turbulent flow downstream, dragging it into the recirculation region to favor mass diffusion, mixing rates and, therefore, combustion performance. It was also found that the main recirculation region is controlled by both Left and Right inlets in two different fashions: the Right inlet "pushes" the flow, including fresh combustion air, inside the recirculating region, whereas the Left inlet transfers some of its momentum to the recirculation motion due

to viscous layers interaction. Furthermore, the Left inlet jets also drag some of the air entrained in the recirculating stream out to the exhaust channel.

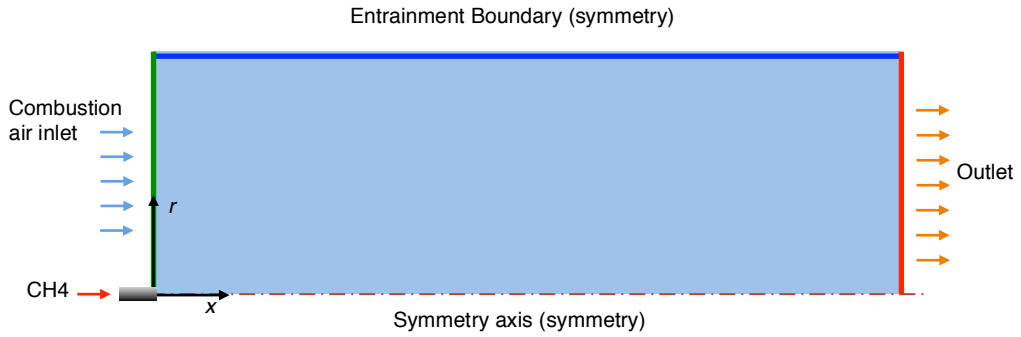

Figure 18 – Numerical domain and boundary conditions enclosing the lifted flame.

A lifted non-premixed turbulent flame was used to validate the reacting flow module on OpenFOAM®. OpenFOAM® computes the reaction rates directly from the chemistry mechanism, equation (2.11), and uses a turbulence/chemistry interaction model, the PaSR model, to resolve the turbulent flame structure. Figure 18 illustrates the axisymmetric numerical domain enclosing the flame. The reference work for this validation is the flame studied experimentally and numerically by Mahmud (2007). It consist of a free jet methane flame discharging into still air through a burner with a inner diameter, D, of 5 mm. In-flame measurements of gas temperature, oxygen and NO concentration are presented in the reference work and compared with the presented results computed with OpenFOAM®.

The computational domain is an axisymmetric plane with the symmetry axis coincident with the axis of the burner. The outlet boundary is located at $200D$ from burner exit and the entrainment boundary, parallel to the symmetry axis, is placed at $50D$ from the axis. Since OpenFOAM® is essentially a finite volume solver, the axisymmetric plane had to be converted into a wedge volume with a very small wedge angle. The volume was created with a revolution transformation of 2.5-degrees centered at the symmetry axis. The numerical grid was discretized with hexahedron elements, except for the row containing the symmetry axis that consisted of wedge elements. The grid had an element density similar to the grids used in Mahmud (2007) and comprises 140 elements in the axial direction and 50 elements in the radial direction. According to Mahmud (2007), this grid configuration is sufficiently fine to reproduce acceptable grid independent solutions.

The solver set-up was the same used to compute the results presented in the previous section, although with chemistry reactions enabled this time. Turbulence was modeled with the standard $k-\varepsilon$ turbulence model with the default constant values. Three chemical

mechanisms were tested – the simplified Westbrook and Dryer 2-step mechanism, the skeleton Smooke mechanism and the detailed GRI-2.11 mechanism. The discrete ordinate method was implemented to solve the radiative heat transfer. The converged solution was considered when continuity, pressure and enthalpy residuals were less then 10^{-8} or when the temperature field remained unchanged for at least 1/3rd of the total simulation time. The under-relaxation factors for the radiative terms were set to 0.5 and the remaining were set to 0.8. It was found that the solver with chemistry enabled had an unstable behavior when the maximum courant numbers of the flow was higher than 0.4. Therefore, the maximum courant number allowed was 0.2, limiting the simulation time-step to $\approx 1.2\times10^{-5}$ seconds. The simulations were carried out in a 16-core cluster set-up and took about 6 and 13 hours to achieve convergence with the 2-step Westbrook and Dryer chemical mechanism and the Smooke mechanism, respectively. However, the solution with the GRI-2.11 scheme was only completed after 1 week of computational time, with the same cluster set-up, underlining the extreme computational cost that the detailed chemical mechanism demands.

A uniform axial velocity profile with magnitude equal to 46.4 m/s and zero radial velocity was imposed at the fuel inlet. At the combustion air inlet, inlet velocity was set to 0.8 m/s in the axial direction. The temperature on both inlet boundaries was set to the ambient temperature T_0 = 293 K. The turbulence fields at the boundaries and at the initial time-step were estimated assuming 10% of turbulent intensity and 1/3rd of the burner radius for the turbulent length scale. Every boundary was considered as a black surface at ambient temperature.

Figure 19 shows the temperature contours of the lift-off flame computed with the Westbrook and Dryer 2-step mechanism, the Smooke mechanism and the GRI-2.11 mechanism, Figure 20 and 21 compare the measurements available in Mahmud (2007) with the radial profiles of temperature and oxygen concentration predictions at different stations located along the length of the flame and Figure 22 exhibits the axial profile of temperature, oxygen and methane along the symmetry axis.

Overall, the estimated temperature and oxygen distribution obtained with the Westbrook and Dryer 2-step scheme and the Smooke scheme were fairly similar over the entire numerical domain, with only residual differences, whereas the solution with the GRI-2.11 mechanism, although also similar near the burner to the solution of the other chemical mechanisms, exhibited a temperature decay in the trailing region of the flame, as observed in the temperature contours and profiles presented.

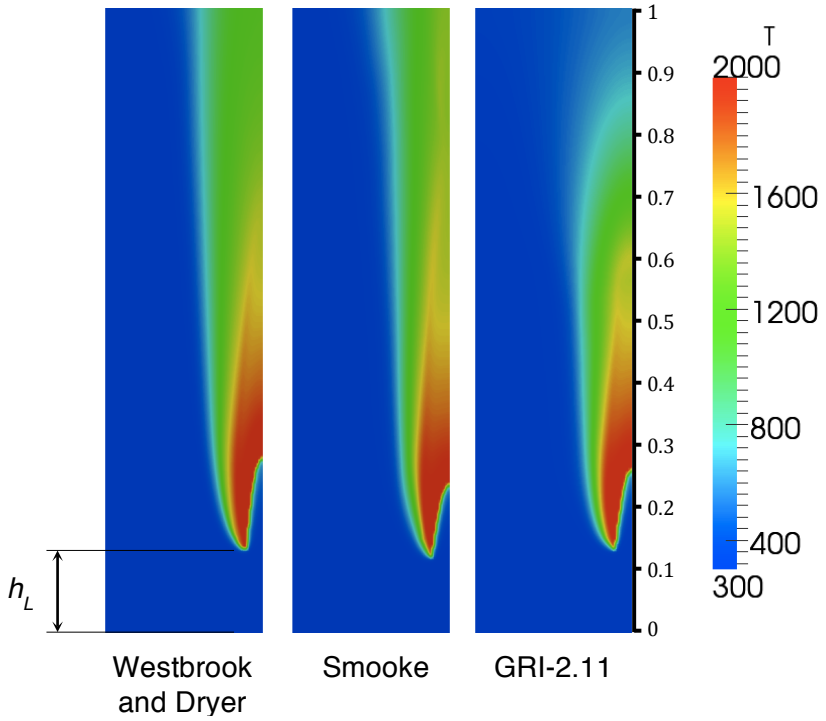

Figure 19 – Temperature contour of the lift-off flame computed with the PaSR model and the Westbrook and Dryer 2-step mechanism, the Smooke mechanism and the GRI-2.11

The lift-off heights resolved numerically, listed on Table 2, show reasonable agreement with the experimental results, indicating that the PaSR combustion model reproduces the detached flame appropriately, regardless the chemical mechanism used. Moreover, the temperature contours on Figure 19 show that a non-reacting region near the symmetry axis penetrates into the flame and pushes the flame front near the axis further downstream. As evidenced in the axial profiles along the symmetry axis of Figure 22, the maximum penetration distance measured in the numerical solutions is roughly between 0.24 and 0.28 m from the burner, depending slightly on the chemical scheme used. Unfortunately, the experimental data available is not enough to locate the maximum penetration of this non-reacting region. In Figure 20 and 21, both the numerical predictions and measurements at station x = 0.2 m are consistent with the previous observations, showing the extended non-reacting region for r < 0.01 m, while in the region 0.01 < r < 0.06 m the high temperature gradients indicate the development of the reacting flow.

	Westbrook and Dryer	Smooke	GRI-2.11	Data (Mahmud 2007)
Lift-off height, h_{LO}	0.137	0.128	0.139	0.127

Table 2 – Lift-off heights measured from the numerical results and determined from the experimental data

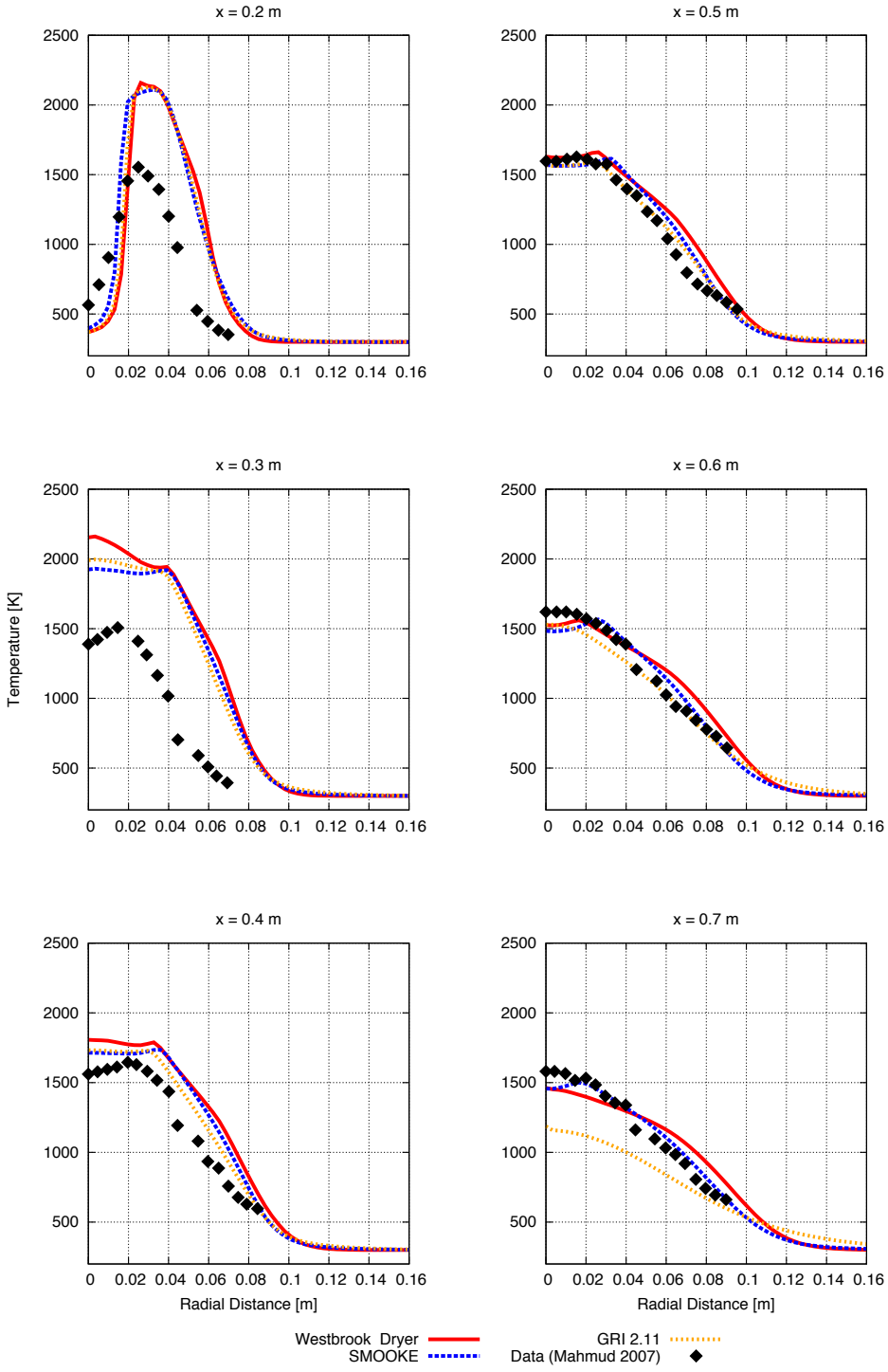

Figure 20 – Predicted and measured radial profiles of the mean gas temperature at various stations along the length of the flame.

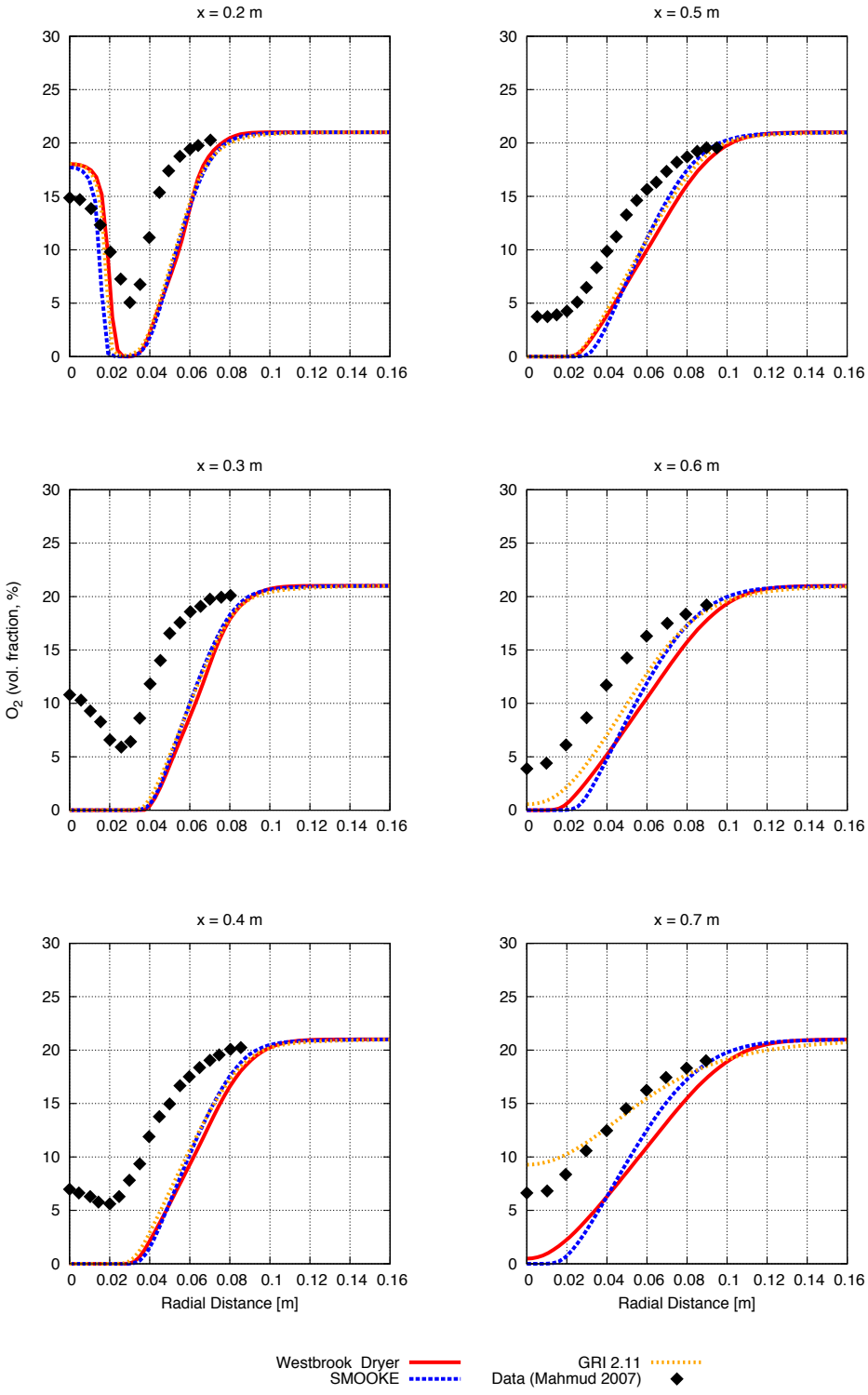

Figure 21 – Predicted and measured radial profiles of the oxygen volume concentration at various stations along the length of the flame.

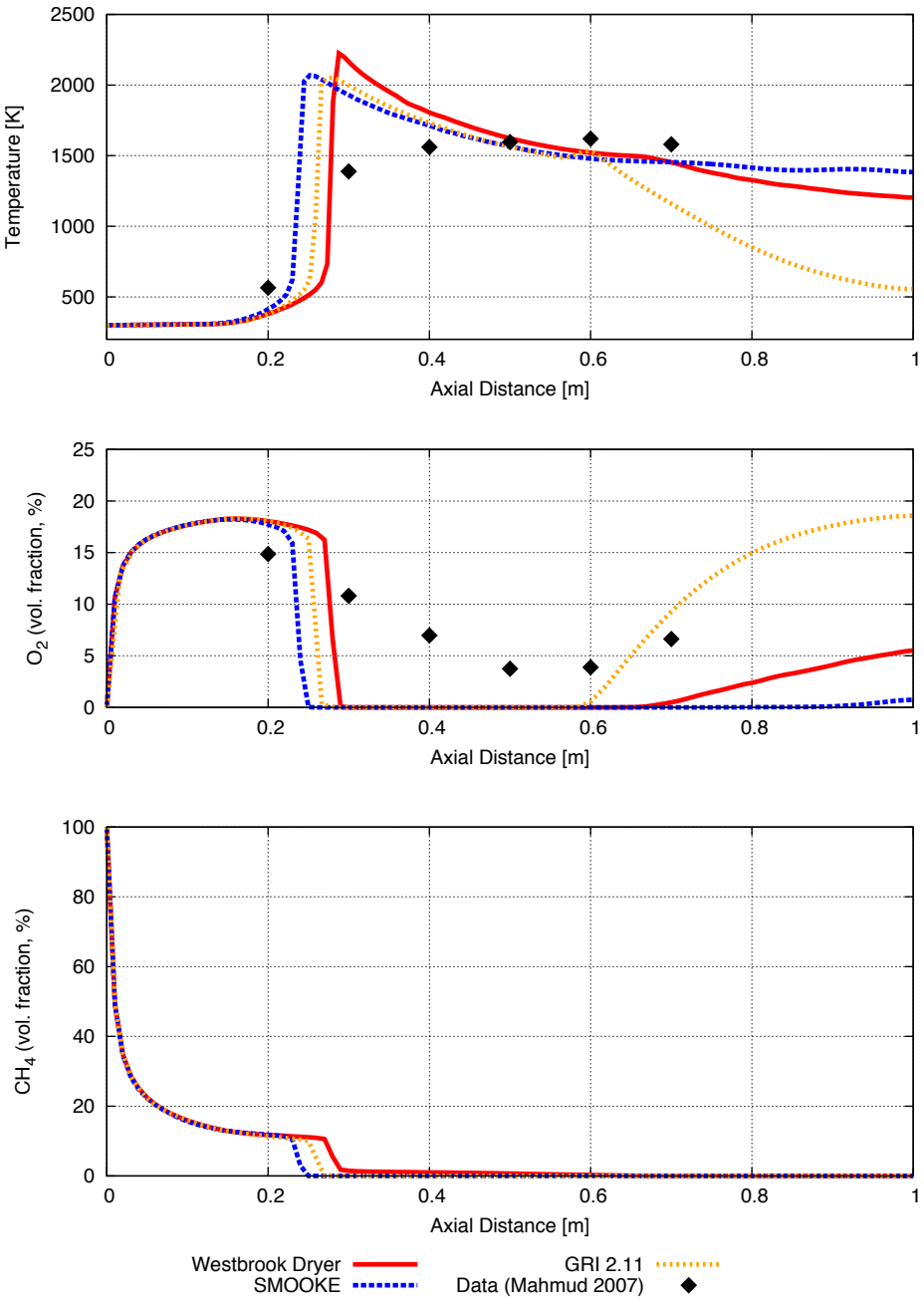

Figure 22 – Predicted and measured axial profiles of the mean gas temperature along the length of the flame.

At stations x = 0.2 m and x = 0.3 m in Figure 20, the temperature profiles are appreciably higher than the experimental data. Furthermore, the predicted profiles taken along the symmetry axis of the flame, in Figure 22, show a sharp temperature rise at the flame front, while the experimental data yielded a rather smoother temperature rise. Likewise, the oxygen and methane concentration levels at the flame front quickly drop and maintain at virtually null levels inside the flame, despite the experimentally measured oxygen levels show a much

smother evolution and are not lower than 5% at the same locations. The oxygen concentration radial profiles in Figure 21 also yield practically null oxygen levels inside the core of the flame, for $r < 0.02$ m, in the regions closer to the burner, $x < 0.6$ m, as opposed to the experimental data.

The reported results obtained with the PaSR model reveal, in general, relevant inconsistencies with the measured data. On one hand, the sharp depletion of oxygen and methane at combustion onset suggests that the PaSR combustion model severely amplifies the reaction rates in the fuel-rich regions near the burner, resulting that all oxygen and methane available are immediately consumed at the flame front. On the other hand, the reason for the lack of oxygen inside the flame denotes that the numerical model is not be able to capture appropriately the air (and oxygen) entrainment into the flame near the burner, preventing fresh air from reaching the flame core. Likewise, this may also explain the high flame temperatures predicted in the numerical solution, as the dilution of the fresh air surrounding the reacting flow would reduce flame temperatures.

The deficiencies identified previously may be attributed to a combination of the limitations of the combustion model and the turbulence model. It is well known that turbulence and combustion are two strongly coupled phenomena and should be analyzed together. As concluded by Peng (2008) in his work with diesel spray turbulent combustion, one of the reasons for the discrepancies between the numerical and experimental results obtained with the PaSR combustion model is that the effects of air entrainment and air-fuel mixing might not be well formulated, requiring more improvement. He also suggests that the determination of the turbulent mixing time, given by equation (2.44) and repeated bellow, might be incorrect or needs further calibration. In fact, as long as the model constant C_{mix} was lower than 1 (0.1, 0.03 and 0.005 were tested), no tangible differences would be noticeable in the resulting solution.

$$\tau_{mix} = C_{mix}\sqrt{\frac{\mu_{eff}}{\bar{\rho}\varepsilon}} \qquad \text{with } C_{mix} = 0.03 \tag{3.2}$$

As highlighted in equation (3.2), the turbulent mixing time, τ_{mix}, depends on turbulent quantities determined by the turbulence models. Several studies concluded that the $k-\varepsilon$ turbulence model under-predicts the turbulence quantities in the regions of high gradients (Rodi, 1984), recommending an ad-hoc reset of the model constants. They verified that the $k-\varepsilon$ model is responsible for the incorrect prediction of air entrainment into the reacting

flow and the air-fuel mixture process in regions near the burner and, thus, flame strain is considerable under-predicted, leading to a much thinner flame front with sharper temperature and species profiles, as pictured in the present numerical results, rather than much smoother profiles and larger flame fronts, typical of turbulent combustion with high flame strain rates. Further, it is worth mentioning that OpenFOAM® considers a Lewis number and a turbulent Schmidt number of unity to model mass diffusion of species, which, according to Hildberg, *et al.* (2002) can lead to significant errors, namely regarding mass diffusion and air-fuel mixing mechanisms.

At stations x = 0.4 m to x = 0.7 m, the flame core temperature decreases due to the heat flux from the hot burnt gases to the surrounding air, overcoming the combustion heat release. At this stage, the predicted temperature profiles yield good agreement with the measured data. The estimated heat flux appears to be slightly higher comparing with the measurements, as showed in the profiles, particularly at stations x = 0.6 m and x = 0.7 m where the temperature inside the flame core is somewhat lower than the experimental data, whereas the temperature at the outer region is over-predicted. The heat flux from the hot gases to the surrounding fresh air is dominated by the radiative heat fluxes. Despite these marginal differences, the results evidence good performance of the DOM solving the radiative fluxes.

Downstream of station x = 0.7 m, the results with the GRI-2.11 chemical mechanism show a substantial under-prediction of the temperature inside the flame, which does not occur with the solutions obtained with the other mechanisms and is not compliant with the measurements. This behavior might be related to the fact that the GRI-2.11 chemical mechanism includes nitrogen chemistry, namely the thermal-NO and the prompt-NO schemes.

As evidenced in Figure 23, the temperatures considerably high above 1850 K, estimated with the GRI-2.11 chemical mechanism, triggered the intense formation of thermal-NO at the flame front. In addition, the inadequacy of the PaSR model in determining the reaction rates also contributed to the significant over-prediction of NO relatively to the experimental results. The NO is then transported downstream by the flow to the trailing region of the flame. At location x = 0.7, as oxygen becomes available, the incoming NO is re-oxidized, producing NO_2, as illustrated by the dashed-blue line in the plot of Figure 23. Because both oxidations of the atmospheric nitrogen are highly endothermic reactions, it is reasonable to admit that the flame temperature decay is owned to energy (heat) consumption of the chemical oxidation reactions producing NO and NO_2, since the other chemical mechanisms, without nitrogen

chemistry, did not yield the same temperature decay. Moreover, it is believed that the small rise in the NO_2 levels at the symmetry axis before the flame front ($0.2 < x < 0.25$) is due to the re-oxidation of NO that is dragged from flame front regions upstream, away from the symmetry axis, and reacts with the oxygen present in the non-reacting flow near the symmetry axis, as evidenced by the slight decay at $x = 0.15$ of the oxygen levels plotted in Figure 23.

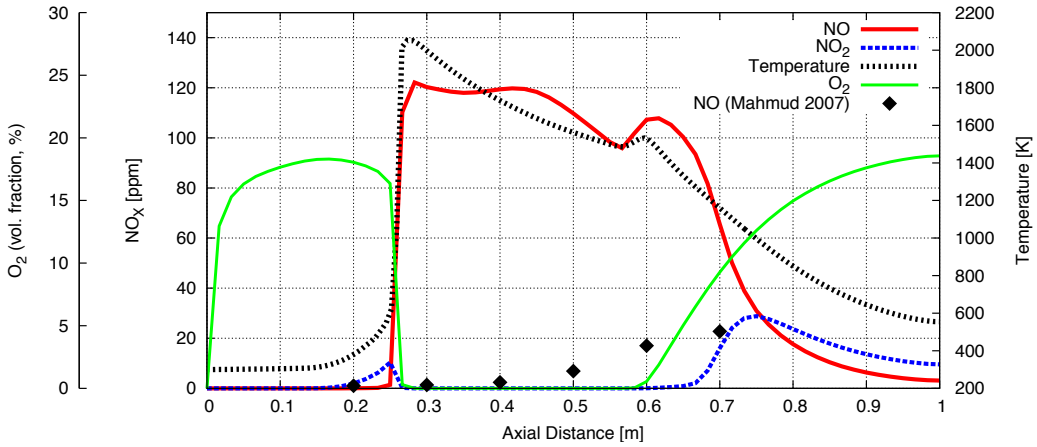

Figure 23 – NO, NO_2, O_2 and temperature predictions and NO experimental measurements along the central axis, obtained using the GRI-2.11 chemical mechanism.

Air entrainment and the air-fuel mixing process are fundamental mechanisms in turbulent combustion and, most importantly, in flameless combustion, in which rapid dilution of combustion air, burnt products and fuel must be ensured so that a homogeneous reacting mixture can be generated before it ignites. Several researchers investigating flameless combustion with the EDC combustion model and the $k - \varepsilon$ turbulence model in a common industrial furnace configuration (see section 1.2) were able to achieve flameless conditions and get reasonable agreement with experimental data of temperature and species distribution, despite the unrealistic results obtained near the burner. Rebola (2010) evaluated the performance of the RSTM model to solve flameless combustion inside an industrial furnace configuration and he found no improvement of the solution near the burner, relatively to the $k - \varepsilon$ turbulence model and the experimental data, adding that the $k - \varepsilon$ model offered better performance overall. These facts emphasize the limitations of the $k - \varepsilon$ turbulence model, and even of the RANS turbulence models in general, in predicting correctly the air-fuel mixing mechanisms, air entrainment and flame strain in the presence of high species concentration gradients and high velocity gradients near the burner. On the other hand, the previous works considered a constant Lewis number equal to 1 and that might constitute a

rather rough assumption in turbulent flames, as pointed out before. Perhaps, these deficiencies might be overcome, on one side, if a more complete description of the Lewis number for each species is considered. On the other side, stronger and more efficient mixing flow configurations, such as cross-flows, counter-flows or recirculation flows, may overlap the deficiencies of the turbulence models which become less relevant on the final solution. The latter alternative is used in the FLOXCOM® combustor concept and will be further discussed in the next section. Finally, LES is known to offer much accurate results in terms of species entrainment and diffusion rates, given that they reproduce the larger eddies, which are the main vehicle for mass diffusion in turbulent flows. In fact, LES was so far an unpractical alternative when applied to complex and large systems, mostly due to the limited computational resources available. However, with the fast increase of computational power, this tendency is changing and more and more researchers favor the LES approach to solve reacting flow over the URANS models.

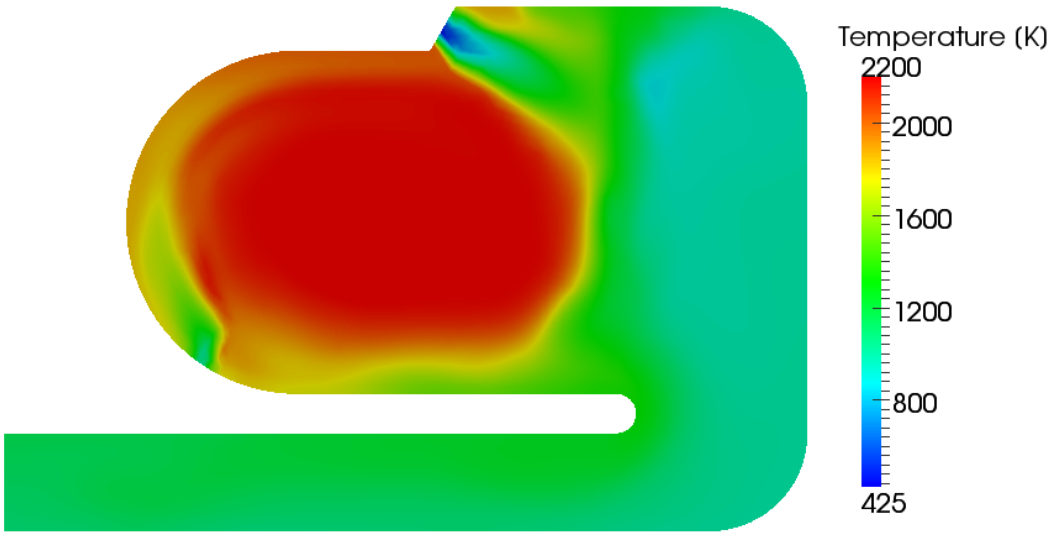

Figure 24 – Predicted temperature contour at the central meridian plane.

The present section features the results of the reacting flow simulation in the FLOXCOM® flameless combustor concept. According to Melo (2006), the operating conditions listed in Table 1 are suitable to create a flameless combustion regime inside the combustor and, therefore, the same operating conditions were reproduced numerically with the PaSR combustion model in OpenFOAM®. The numerical domain was discretized with the grid of Section B. Regarding the chemical mechanism, the skeletal Smooke mechanism revealed as a better compromise to simulate the combustion regime inside the FLOXCOM® combustor. In fact, the remaining chemical mechanisms constitute an inappropriate alternative, inasmuch that the GRI-2.11 chemical mechanism demands excessive computational cost, which is fairly prohibitive for a large system such as the present one and, on the other hand, the simplified 2-steps mechanism proposed by Westbrook and Dryer (1981) does not consider radical formation, which might be relevant to simulate the slow chemistry of flameless combustion.

The numerical procedure carried out to obtain the converged solution of the reacting flow comprised two steps: (I) starting with the non-reacting flow solution presented in section 3.1 as initial solution, the reacting flow computation was carried out with the standard $k-\varepsilon$ turbulence model until the solution became statistically stable. Radiation is disabled at this stage. Then, (II) using the solution obtained previously, the simulation was restarted with the RSTM turbulence model and the P_1-approximation to solve the radiative heat equation.

A numerically emulated ignition was implemented in the code to initiate chemical reactions. For this, an enthalpy source was added to a small amount of cells, roughly in the same region and containing a flammable mixture. The enthalpy source had to be high enough to keep the temperature of the mixture higher than the auto-ignition temperature of the fuel and start the chemical reactions. As soon as the reacting volume was large enough to maintain combustion, the enthalpy source was cancelled. This process took about 10000 time-steps to completion, corresponding to 20 milliseconds of simulated time.

The solver, the PDE's discretization methods and boundary conditions applied in the non-reacting simulations were repeated for the current simulation. Additionally, concerning the radiation flux calculations, the walls were treated as opaque and diffusive, with emissivity set to 0.7. According to Levy (2004), the FLOXCOM® concept was devised considering adiabatic walls and, therefore, the heat flux through the walls was neglected and a zero-gradient boundary condition was assigned for temperature at the walls. Not withstanding, since adiabatic conditions are impossible to reproduce experimentally, the measurements obtained by Melo (2006) were affected by heat loss and, as a result, the numerical solution will certainly over-predict them. The under-relaxation factors addressed to the momentum and energy equations were 0.5, whilst the radiative heat equation solution was relaxed by a factor of 0.4. The transient solution was limited by a Courant number of 0.4 to keep the solution from diverging, resulting in a time-step of $\approx 2.6\times10^{-6}$ seconds.

Figure 24 to 27 show the contours of the predicted temperature field, concentration levels of some relevant species and velocity distribution at the central meridian plane.

In Figure 24 to 26, the temperature and species contours inside the FLOXCOM® combustor clearly evidence the presence of a large, high temperature region with uniform temperature and species distribution, corresponding to the reaction region of the combustor. From Figure 27 is also evident the strong recirculation motion of the reaction region. Furthermore, Figure 25 indicates that the reaction zone is scarce in oxygen but rich in combustion products. These features are consistent with the working principles of the FLOXCOM® combustor, as stated by Levy (2004), which result in a flameless combustion mode and ultra-low NO_x emissions.

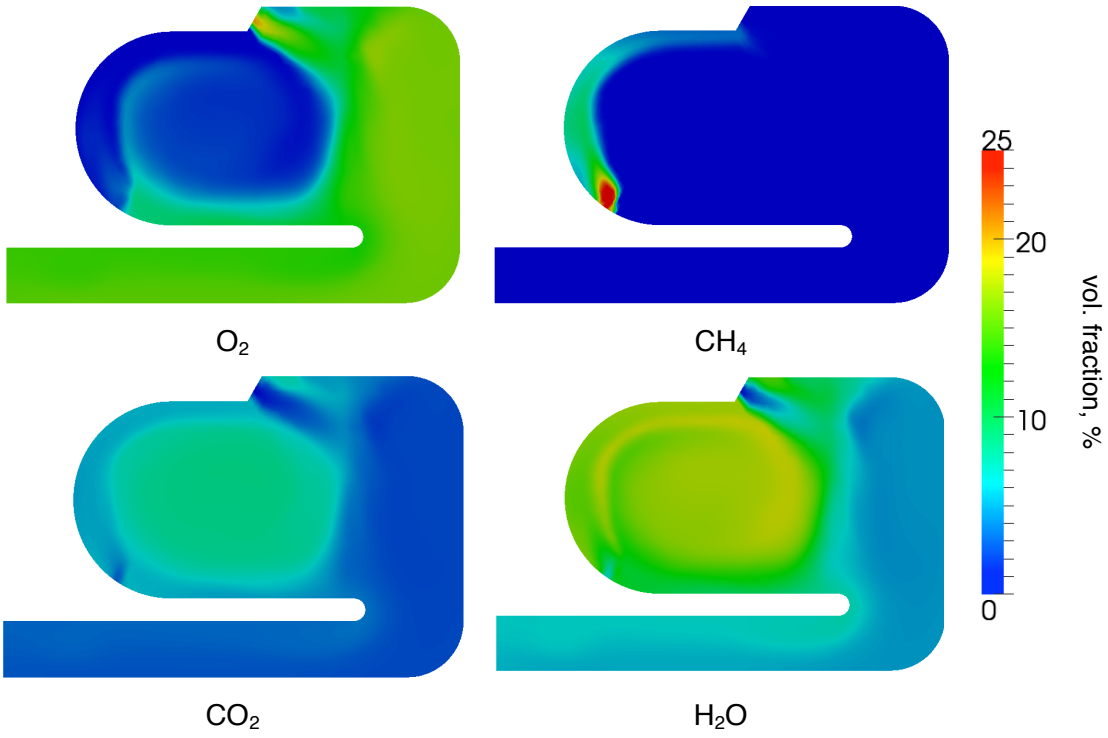

Figure 25 – Predicted concentration levels of O_2, CH_4, CO_2 and H_2O at the central meridian plane.

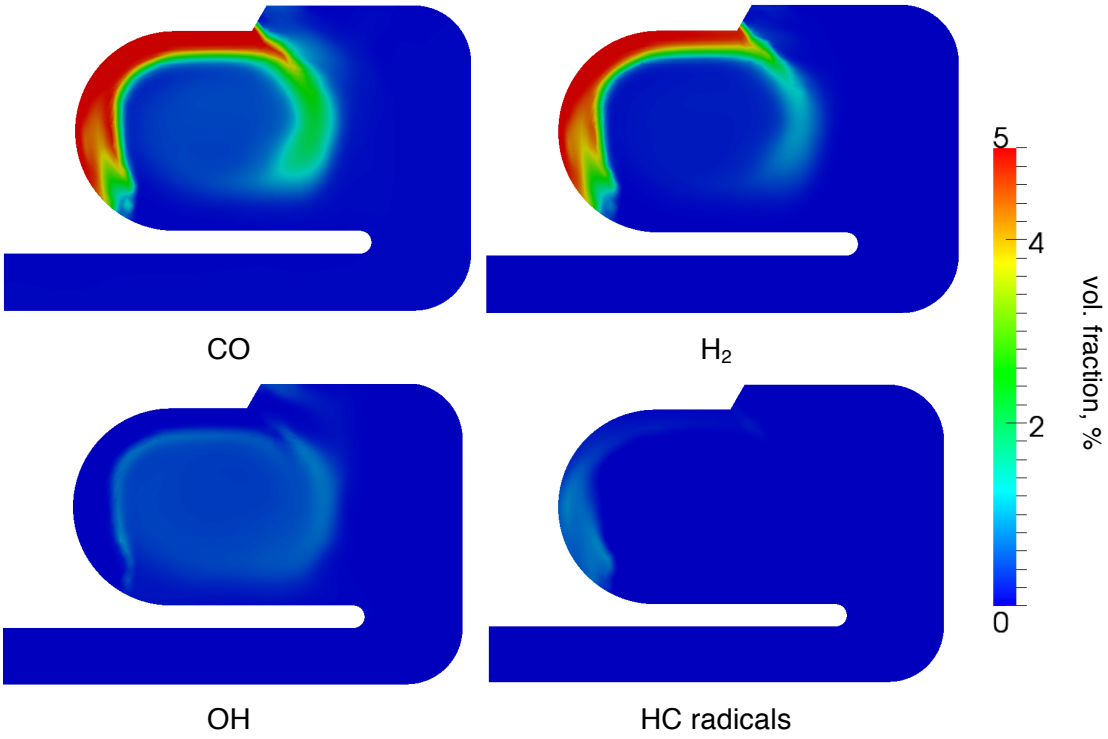

Figure 26 – Predicted concentration levels of CO, H_2, OH and hydrocarbon free radicals (HC) at the central meridian plane.

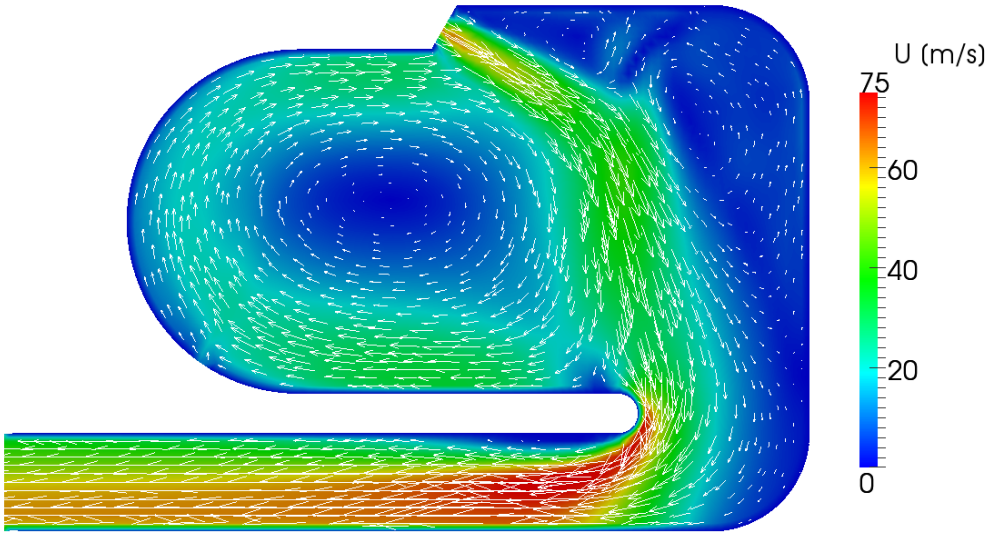

Figure 27 – Predicted velocity contour and vector orientation at the central meridian plane.

As shown in Figure 25, the recirculating motion entrains the fresh combustion air at the combustor entrance and drags it around the reaction region, next to the combustor walls. Simultaneously, the temperature of the entrained fresh air increases as it is diluted with the burnt gases carried by the recirculating flow. As pictured in the contour of Figure 25, the oxygen is not evenly stirred in the burnt combustion products before the fuel is injected in the flow, whereas, according to the FLOXCOM® combustor working principles, fresh air and combustion products should be well diluted with each other at that stage. The excessive oxygen levels increase reaction rates locally, disrupting the uniform profile of temperature and species required for effective flameless combustion. No conclusion can be drawn with the present results about the source of this inconsistency and further investigation is necessary to determine if it is due to the inappropriate calculation of air entrainment and mass diffusion rates or if it is own to the actual aerodynamic characteristics of the combustor, indicating that the fuel is injected prematurely.

Just downstream the fuel inlet, one can identify a region where high methane levels (above 25% in volume fraction) expand over a significant wide area, considering the very small diameter of the fuel injector, suggesting substantial methane diffusion rates in the recirculating flow. Furthermore, the recirculating flow entrains and dilutes a relevant amount of methane (about 10% in volume fraction), as it penetrates into the recirculation region. This might be an indication that the strong fuel jets injecting perpendicularly to the main recirculating flow greatly enhance mass diffusion and the mixing rates between the combustion mixture (air + recirculated combustion products) and methane. Therefore, with the cross-flowing air and fuel streams configuration, air-fuel mixing mechanisms might

become much more efficient, as observed. Consequently, due to the strong and fast recirculating flow and to the more efficient mixing mechanism, the combustion reactions spread over a wider region, starting just downstream the fuel injector and along the combustor wall, where the methane is first reduced through the intermediate combustion reactions producing H_2, CO, OH and other HC free radicals (Figure 26), to the interior of the reacting region where combustion is completed, liberating CO_2 and H_2O. Even though a large reaction zone might evidence excessive flame strain rates, which typically lead to unstable combustion and eventually blow-off, the recirculating region is able to hold combustion mostly because the temperature of the vitiated flammable mixture is above the auto-ignition temperature of the fuel. In fact, as seen in Figure 24, as the fuel at ambient temperature is injected in the recirculating motion, fast diffusion and mixing rates allow the flammable mixture temperature to increase immediately close to 1200 K, well above the methane auto-ignition temperature (typically 853 K) as expected. Given the uncertain validity of the present numerical model highlighted in the preceding section, it is not possible to confirm the slow reaction rates resulting from the low oxygen content in the reaction zone and to speculate if the computed residence time is enough for complete combustion, accordingly.

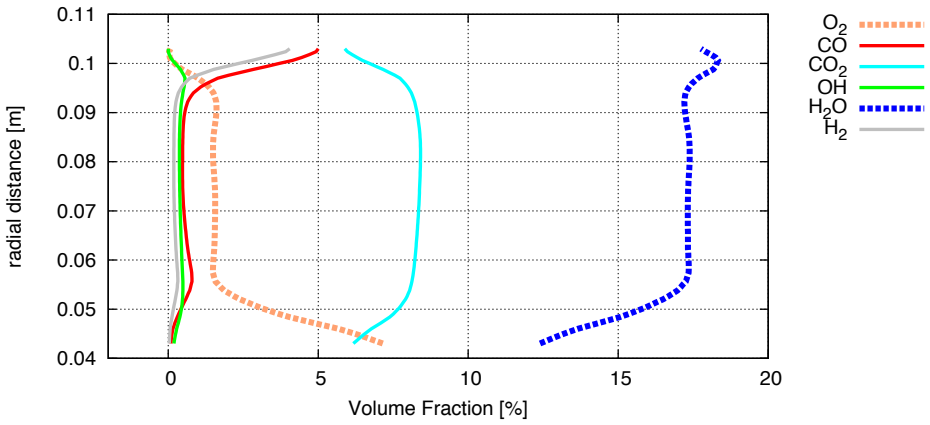

Figure 28 – Radial profile at the center of the reacting region (z = 0.09 m, θ = 0º and 0.043 < r < 0.103 m) of the concentration levels of the species shown in Figures 25 and 26

Examining the contours of Figure 25, apparently the core of the reaction region consists essentially of the products of complete combustion (H_2O and CO_2), atmospheric nitrogen (not represented but, as no nitrogen chemistry was considered in the numerical set-up, it behaved like a inert gas and, thus, is present in the mixture) and practically null oxygen levels. Figure 28 shows a radial profile at the center of the reacting region (z = 0.09 m, θ = 0º and 0.043 < r < 0.103 m) of the concentration levels of the species shown in Figures 25 and 26. As verified in the Figure 28, the oxygen levels profile in the core of the reaction zone are, in fact, roughly

constant for $0.058 < r < 0.093$ m and not lower than 2% in volume fraction. Moreover, the levels of the remaining species are also roughly uniform at the same location, emphasizing the homogeneity of the reaction zone.

Overall, the observations highlighted in the preceding paragraphs showed that the present numerical set-up with the RSTM turbulence model reproduced appropriately the species entrainment to and within the reaction zone and captured the enhanced mixing mechanisms provided by the proper aerodynamics of the combustor, namely the air-fuel mixture process as a result of the perpendicular fuel injection into the flow. The solution obtained with the $k-\varepsilon$ model, not represented here, failed to reproduce those mechanisms, yielding, for instance, virtually null oxygen concentration levels inside the reaction zone. This highlights the limitations of the $k-\varepsilon$ model in predicting diffusion rates and species entrainment in reacting flows.

Despite the numerical model, with the RSTM turbulence model, properly reproduced the mixing mechanisms and species entrainment, the estimated temperature distribution in the reaction region is still much higher than the experimental data. In fact, Figure 24 and the right plot of Figure 29 reveal an average temperature around 2200 K, whereas the maximum temperature registered by Melo (2006) was about 1850 K (Figure 29), which is the known temperature threshold from which intensive thermal-NO formation is triggered. As outlined before, this might be owned to the fact that heat loss through the walls is disregarded in the numerical model and to the incorrect prediction of the reaction rates as a result of the inadequate treatment of the turbulence/chemistry interaction formulated in the combustion model.

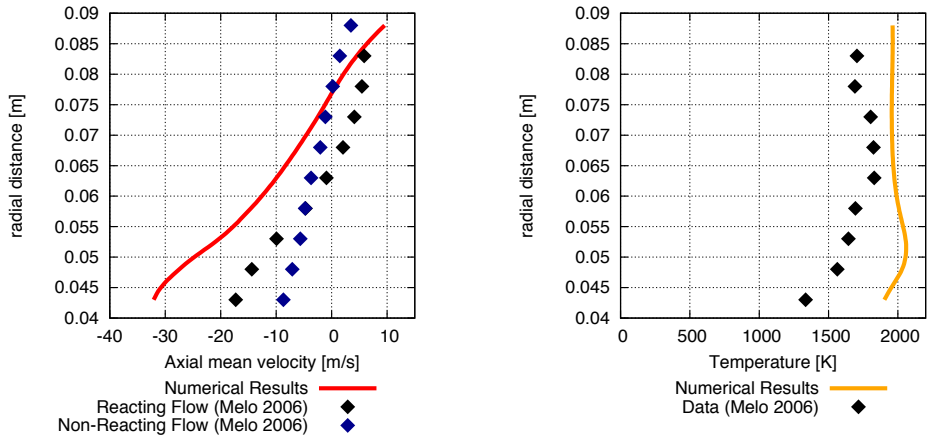

Figure 29 – Data and predicted results of the axial velocity and temperature profiles at the center of the recirculation region ($z = 0.09$ and $\theta = 0^{o}$). The uncertainty of the temperature measurements is about 5% (Melo, 2006).

Comparing Figure 27 with the velocity contour at the central meridian plane for the non-reacting flow showed in Figure 15, one can clearly observe that the secondary recirculating flow, developed in the non-reacting flow, has relatively less strength in the reacting flow. On the other hand, the numerical results indicate that the strength of the main recirculating flow is significantly higher in the reacting flow. As Figure 29 evidences, this behavior is consistent with the experimental observations, although the numerical solution considerably over-predicts the momentum of the recirculation flow. It is believed that the latter over-prediction is related to the higher temperature field resolved by the combustion model which induce extra thermal expansion of the fluid and, therefore, greater velocities. Nevertheless, further investigation should be carried out to fully understand the complexity of these relations. Consequentially, the averaged recirculation rate determined with the numerical results and taken at different locations of the recirculation region was 17,4, as opposed to the recirculation rates of 0.75 determined by Melo (2006) for the same combustor prototype. Even though Melo (2006) only provided an estimation of the recirculation rate, the discrepancy between the measured data and numerical solution are still rather important.

The velocity vector orientation in Figure 27 indicate that a large amount of inlet air is directed straight the dilution exhaust. The considerable oxygen levels at the exhaust channel, as shown in Figure 25, stress that a substantial amount of unburnt air, rich in oxygen, is leaving the combustor. As mentioned previously, this is an important flow feature of a GT combustor and corresponds to the dilution air that decreases the temperature of the exhaust combustion products and homogenizes the temperature profile at the outlet, protecting the first stage turbine blades from excessive thermal wear.

Overall, although the results show poor agreement with the experimental data, qualitatively, they feature the fundamental working conditions of the FLOXCOM® flameless combustor concept, established by Levy (2004). In addition, the numerical model of the reacting flow, with the RSTM turbulence model resolving the turbulent flow, captured appropriately the aerodynamic characteristics of the reacting flow inside the FLOXCOM® combustor, namely the efficient mixing mechanisms and species entrainment.

CHAPTER 4

CONCLUSIONS AND FUTURE WORK

4.1 Conclusions

This work comprised the study of the reacting and non-reacting flow inside a FLOXCOM® GT combustor prototype for an aircraft application, devised by Levy (2004) and characterized experimentally by Melo (2006). The analysis focused on the performance of the numerical model established, with emphasis to the reacting flow characteristics and the mixing mechanisms. The results were compared with the experimental data available for the simulated combustor. The turbulence/chemistry interaction was treated with the PaSR combustion model, implemented in OpenFOAM®, which was also validated in this work. In the non-reacting flow analysis, a detailed characterization of the aerodynamics in the combustor was carried out. In addition, the effects of the grid and the standard $k-\varepsilon$ model and RSTM turbulence models on the numerical solution were also examined. The validation the PaSR combustion model involved the reproduction of a lifted, non-premixed, turbulent free jet flame described experimentally in Mahmud (2007). Three chemical mechanisms were used along the combustion model, namely the 2-step Westbrook and Dryer mechanism, the skeletal Smooke mechanism and the detailed GRI-2.11 mechanism. Turbulence was modeled with the standard $k-\varepsilon$ model and the radiation fluxes were determined with the method of

discrete ordinates. The work concluded with the analysis of the reacting flow inside the FLOXCOM® combustor prototype.

The numerical results and their discussion lead to the following conclusions:

A. The effect of the turbulence models and the three meshes analyzed, comprising 39508, 109384 and 253878 cells, is fairly residual on the numerical solution. Nevertheless, the case that better reproduced the experimental results was the solution of Section C with the RSTM turbulence model.
B. In the non-reacting flow, one can identify two recirculating motions: the main recirculation flow occupying most of the combustor's volume and a secondary recirculating flow attached to the Right inlet. It is believed that the secondary flow drains most of the momentum carried by the Right inlet jet and, therefore, it is an unwanted behavior.
C. The Right inlet jet is responsible to "push" fresh combustion air towards the recirculating region, while the Left inlet jets entrain a portion of the recirculating air towards the exhaust channel and transfers some of its momentum to the recirculation motion, due to the viscous effects.
D. The interaction between both the Left an Right inlet jets allows some of the inlet fresh air to be directed straight to the dilution channel to cool down the exhaust gases and homogenize the exit temperature profile.
E. In the lift-off turbulent flame simulation, the numerical solution over-estimates, in general, the reaction rates, leading to unrealistic temperature profiles. It is believed that this fact as to do with a wrong calibration of the combustion constants, or inappropriate formulation of the turbulence mixing time, and to the incorrect prediction of turbulent quantities by the turbulence models.
F. The scarcity of oxygen inside the lifted flame and the high flame temperatures suggest that the numerical model could not predict correctly air entrainment into the interior of the flame. Several researchers confirmed this behavior and identified the reason as being the ineffectiveness of the $k - \varepsilon$ turbulence model in reproducing these effects in a reacting-flow.
G. Regardless the shortcomings of the turbulence/chemistry interaction model, the lift-off heights computed with either chemical mechanism showed reasonable agreement with the experimentally measured value.
H. The numerical solution of the reacting flow inside de FLOXCOM® combustor, with the RSTM turbulence model, reproduced appropriately the species

entrainment to and within the reaction zone and captured the enhanced mixing mechanisms provided by the aerodynamics of the combustor.

I. The combustion air dragged into the reacting flow is not completely diluted with the burnt products before fuel is injected. This may be own to the insufficient prediction of mass diffusion by the numerical model or to the actual aerodynamics of the combustor.

J. The temperature distribution and concentration levels of species inside the recirculating reaction region were reasonably uniform, emphasizing the homogeneity of the reaction zone, as expected.

K. The results showed that the numerical set-up with the RSTM turbulence model reproduced properly the species entrainment within the reaction zone whilst the solution obtained with the $k - \varepsilon$ model did not, stressing the shortcomings of the latter model in predicting mass diffusion and species entrainment, relevant for reacting flow simulations.

L. The temperature field determined for the reacting flow inside the FLOXCOM® combustor was considerable over-estimated, regardless the use of the RSTM turbulence model. Consequently, the velocity field in the reaction zone was also over predicted due to the greater thermal expansion induced by the higher temperature field. The disregard of heat loss through the combustor walls and the incorrect prediction of the reaction rates, as a result of the inadequate treatment of the turbulence/chemistry interaction formulated in the PaSR combustion model, might explain the high temperature values, well above the 1850 K threshold of NO_x production.

M. Despite the over estimated temperature distribution, the numerical model of the reacting flow was able to reasonably reproduce most of the features of the FLOXCOM® combustor concept appropriate for flameless combustion, devised by Levy (2004).

Overall, the numerical model was not sufficient to solve the temperature profiles and the air-fuel mechanisms in the reacting flow, mostly due to the inappropriate formulation of the combustion model. On the other hand, the non-reacting flow was well predicted by the numerical model with the $k - \varepsilon$ model and the RSTM turbulence models.

4.2 Future Works

Given the latter conclusions, further improvement of the combustion model implemented in OpenFOAM® is necessary. As emphasized in the preceding conclusions, a reformulation of the model is necessary to contemplate with more precision the turbulence/chemistry interaction processes. Also, the use of more detailed turbulence descriptions, like the LES approach, might conduct to better prediction of the mixing mechanisms and air entrainment, however, at a greater computational cost.

A good alternative to the PaSR combustion model should be the EDC combustion model that has proven potential in predicting flameless combustion. Thus, the implementation of the EDC combustion model into OpenFOAM® could be also considered as a future goal. It would be of great value to repeat this investigation with the EDC combustion model and verify if the results exhibit some improvement and if they are compliant with the measured data.

The issue of heat loss through the wall might be also a topic of discussion in future studies, especially when a more precise combustion model is in hands. However, this implies repeating the whole experimental apparatus and measure the heat loss. This is a cumbersome task and alternative solutions should be found. One alternative could involve the projection of a heat loss factor based on data available in the literature for a similar combustor with roughly the same power output.

Even though the GRI-2.11 chemical mechanism included nitrogen chemistry, it demands excessive computational cost and becomes unpractical for current use. Thus, a plausible solution is the use of a simplified chemical mechanism for the fuel oxidation chemistry and a post-processing NO model to estimate the nitrogen chemistry as described in Ma, *et al.* (2000), and often used by other researchers in combustion research, namely, in flameless combustion simulations.

Finally, as the simulation set up achieves a mature state, it constitutes a great tool to explore closely and in detail the combustion regime inside a FLOXCOM® combustor, identify any weaknesses and its sources in the present design and promptly analyze different configurations, until an optimum design is attained.

BIBLIOGRAPHY

Arghode, V. H., Gupta, A. K., & Yu, K. H. (2009). Colorless Distributed Combustion (CDC): Effect of flowfield configuration. *47th AIAA Aerospace Sciences Meeting Including the New Horizons Forum and Aerospace Exposition.* Orlando, Florida.

Christo, F. C., & Dally, B. B. (2005). Modeling turbulent reacting jets issuing into a hot and diluted coflow. *Combustion and Flame , 142*, 117-129.

Cohen, H., Rogers, G. F., & Saravanamuttoo, H. I. (1996). *Gas Turbine Theory* (4th Edition ed.). U. K.: Longman.

Coppalle, A., & Vervisch, P. (1983). The total emissivities of high-temperature flames. *Combustion and Flame , 49*, 101-108.

Fiveland, W. A. (1984). Discrete-ordinates solution of radiative transport equation for rectangular enclosures. *Journal of Heat Transfer , 106* (699-706).

Gibson, M. M., & Launder, B. E. (1978). Ground Effects on Pressure Fluctuations in the Atmospheric Boundary Layer. *Journal of Fluid Mechanics , 86* (3), 491-511.

Gran, I. R., & Magnussen, B. F. (1996). A numerical study off a bluff-body stabilized diffusion flame, Part 2: Influence of combustion modeling and finite-rate chemistry. *Combustion Science and Technology , 119*, pp. 129-135.

Hilberg, R., & Thévenin, D. (2002). Autoignition of turbulent nonpremixed flames investigated using direct numerical simulations. *Combustion and flame , 128*, 22-37.

Hirsch, C. (2007). *Numerical Computation of Internal & External Flows, Vol. 1 Fundamentals of Computational Fluid Dynamics* (Second Edition ed.). Elsevier.

Joannon, M., Langella, G., Beretta, F., Cavaliere, A., & Noviello, C. (1999). Mild Combustion: Process Features and Technological Constrains. *Proceedings of Mediterranean Combustion Symposium.*

Jones, W. P., & Launder, B. E. (1972). The prediction of laminarization with a two-equation model of turbulence. *International Journal of Heat and Mass Transfer , 55*, 310-314.

Karlsson, J. A. (1995). *Modelling Auto-Ignition, Flame Propagation and COmbustion in Non-stationary Turbulent Sprays.* PhD thesis, Chalmers University of Technology, Göteborg.

Katsuki, A., & Hasegawa, T. (1998). The science and technology of combustion in highly preheated air. *Proceeding of the Combustion Institute.*

Launder, B. E., & Sharma, A. (1974). Application of the Energy-Dissipation Model of Turbulence to the Calculation of Flow Near a Spinning Disk. *Letters in Heat and Mass Transfer , 1*, 131-138.

Launder, B. E., Reece, G. J., & Rodi, W. (1975). Progress in the Development of a Reynolds-Stress Turbulence Closure. *Journal of Fluid Mechanics , 63* (3), 537-566.

Levy, Y., Sherbaum, V., & Arfi, P. (2004). Basic thermodynamics of FLOXCOM, the low-NOx gas turbines adiabatic combustor. *Applied Thermal Engineering , 24*, 1593-1605.

Lefebvre, A. H., & Ballal, D. R. (2010). *Gas Turbine Combustion* (3rd Edition ed.). New York: CRC Press.

Nordin, P. A. (2001). *Complex Chemistry Modeling of Diesel Spray Combustion.* PhD thesis, Chalmers University of Technology, Dept. of Thermo and Fluid Dynamics, Göteborg.

Ma, C. Y., Mahmud, T., Hampartsoumian, E., J., R., & Gaskell, P. (2000). Mathematical modeling of nitric oxide formation in turbulent diffusion flames doped with a nitrogen compound. *Combustion Science and Technology , 160*, 347-367.

Magnussen, B. F., & Hjertager, B. H. (1976). On mathematical modeling of turbulent combustion with spetial enphasis on soot formation and combustion. *Proceedings of the Combustion Institute*, *16*, pp. 719-729.

Mahmud, T., Sangha, S. K., Costa, M., & Santos, A. (2007). Experimental and computational study of a lifted, non-premixed turbulent free jet flame. *FUEL , 86*, 793-806.

Marshak, R. E. (1947). Note on sperical harmonics method applied to the Milne problem for a sphere. *Phys. Rev. , 71*, 443-446.

Melo, M. J. (2006). *Desenvolvimento e Optimização de uma Câmara de Combustão para Turbinas a Gás.* PhD thesis, Instituto Superior Técnico, Departamento de Engenharia Mecãnica.

Melo, M. J., Sousa, J. M., Costa, M., & Y., L. (2009). Experimental Investigation of a Novel Combustor for Gas Turbines. *Journal of Propulsion and Power , 25* (3), 609-617.

Modest, M. F. (1976). Photon-gas formulations of the differential approximation in radiative transfer. *Letters in Heat and Mass Transfer , 3*, 111-116.

Modest, M. F. (2003). *Radiative Heat Transfer* (Second Edition ed.). Academic Press.

OpenCFD. (2011). *OpenFOAM*. Retrieved from http://www.openfoam.com/

Parente, A., Galletti, C., & Tognotti, L. (2008). Effect of the combustion model and kinetic mechanism on the MILD combustion in an industrial burner fed with hydrogen enriched fuels. *International Journal of Hydrogen Energy , 33*, 7553-7564.

Peng, F. K. (2008). *Numerical Modeling of Diesel Spray Injection, Turbulence Interaction and Combustion.* PhD thesis, Chalmers University of Technology, Dept. of Applied Mechanics, Göteborg.

Penner, J. E., Lister, D. H., Griggs, D. J., Dokken, D. J., & McFarland, M. (2000). *Aviation and the Global Atmosphere - A Special Report of IPCC working Groups I and III.* IPCC. Cambridge: Cambridge University Press.

Poinsot, T., & Veynante, D. (2001). *Theorectical and Numerical Combustion.* Edwards, Inc.

Pope, S. B. (2000). *Turbulent Flows.* Cambridge University Press.

Smith, G. P., M., G. D., Frenklach, M., Moriarty, N. W., Eiteneer, B., Goldenberg, M., et al.. Retrieved from http://www.me.berkeley.edu/gri_mech/

Smith, T. F., Shem, Z. F., & Friedman, J. N. (1982). Evaluation of coefficients for the weighted sum of gray gases model. *Journal of Heat Transfer , 104*, 602-608.

Smooke, M. D. (1991). Reduced Kinetics Mechanism and Asymptotic Approximation for Methane-Air Flames. *Lecture Notes in Physics. 384.* Berlin: Springer-Verlag.

Rebola, A. J. (2010). *Investigação Experimental e Computacional de uma Câmara de Combustão Laboratorial Operando no Regime de Combustão sem Chama Visível.* PhD thesis, Instituto Superior Técnico, Depeartamento de Engenahria Mecânica.

Rodi, W. (1984). *Turbulence Models and their applications to hydraulics.* Amsterdam: International Association for Hydraulic Research.

Rotta, J. C. (1951). Statistische Theorie nichthomogener Turbulenz. *Zeitschrift fur Physik , 129*, 547-572.

United Nations Framework Convention on Climate Change (UNFCCC). (2011). *GHG database*. Retrieved from http://unfccc.int/ghg_data/ghg_data_unfccc/items/4146.php

U.S. Department of Transportation. (2010). *Transportation GHG Emissions and Trends*. Retrieved from http://climate.dot.gov/ghg-inventories-forcasts/national/us-inventory-structure.html

Westbrook, C. K., & Dryer, F. L. (1981). Simplified Reaction Mechanism for the Oxidation of Hydrocarbon Fuels in Flames. *Combustion Science and Technology , 27*, 31-43.

Wünning, J. A., & Wünning, J. G. (1997). Flameless Oxidation to Reduce Thermal NO-Formation. (E. Science, Ed.) *Prog. Energy Combustion, Sci , 23*, 81-94.

Wilcox, D. C. (2006). *Turbulence Modeling for CFD* (Third Edition ed.). DCW Industries.

Zeldovich, Y. B., Sandovnikov, P. Y., & Frank-Kamenetski, D. A. (1947). *Academy if Sciences of USSR* .

ATTACHMENTS

A. FLOXCOM® PROTOTYPE DETAILED DRAWINGS